Journal of Manufacturing Processes 108 (2023) 529–550

Contents lists available at ScienceDirect

Journal of Manufacturing Processes

journal homepage: www.elsevier.com/locate/manpro

Online thermal field prediction for metal additive manufacturing of thin walls

Yifan Tang [a], Mostafa Rahmani Dehaghani [a], Pouyan Sajadi [a], Shahriar Bakrani Balani [b], Akshay Dhalpe [b], Suraj Panicker [b], Di Wu [b], Eric Coatanea [b], G. Gary Wang [a,*]

[a] Product Design and Optimization Laboratory, Simon Fraser University, Surrey, BC, Canada
[b] Faculty of Engineering and Natural Sciences, Automation Technology and Mechanical Engineering, Tampere University, Tampere 33720, Finland

ARTICLE INFO

Keywords:
Thermal field prediction
Online prediction
Artificial neural network
Reduced order model
Extreme learning machine
Metal additive manufacturing

ABSTRACT

Various data-driven modeling methods have been developed to predict the thermal field in metal additive manufacturing (AM). The generalization capability of these models has been shown with simulation, but rarely tested with online physical printing. Instead, this paper aims to study a practical issue in metal AM, i.e., *how to predict the thermal field of yet-to-print parts online when only a few sensors are available*. This work proposes an online thermal field prediction method using mapping and reconstruction, which could be integrated into a metal AM process for online performance control. Based on the similarity of temperature curves (curve segments of a temperature profile of one point), the thermal field mapping applies an artificial neural network to estimate the temperature curves of points on the yet-to-print layer from measured temperatures of certain points on the previously printed layer. With measured/predicted temperature profiles of several points on the same layer, the thermal field reconstruction proposes a reduced order model (ROM) to construct the temperature profiles of all points on the same layer, which could be used to build the temperature field of the entire layer. The training of ROM is performed with an extreme learning machine (ELM) for computational efficiency. Fifteen wire arc AM experiments and nine simulations are designed for thin walls with a fixed length and unidirectional printing of each layer. The test results indicate that the proposed prediction method could construct the thermal field of a yet-to-print layer within 0.1 s on a low-cost desktop computer (Intel Core i7-3770 CPU @ 3.40GHz processor, 24.0 GB RAM). Meanwhile, the method has acceptable generalization capability in most cases from lower layers to higher layers in the same simulation, as well as from one simulation to a new simulation on different AM process parameters. More importantly, after fine-tuning the proposed method with limited experimental data, the relative errors of all predicted temperature profiles on a new experiment are sufficiently small, which demonstrates the applicability and generalization of the proposed thermal field prediction method in online applications for metal AM.

1. Introduction

In metal additive manufacturing (AM), the metallic material (e.g., powder or wire) is heated by the energy source (e.g., laser, electron beam, and electric arc) and melted to liquid, after which it cools down and solidifies. Then the deposited material is re-heated by the heat input on the higher layers and then cools down, which is repeated until the part is printed completely. The thermal behavior encountered during printing affects the final properties of the part significantly. For instance, a larger thermal gradient would bring unacceptable residual stresses and thermal distortion, resulting in part failure [1], while a smaller thermal gradient and cooling rate could reduce the hardness of a part [2].

To maintain stable part qualities in metal AM, various data-driven methods have been developed to predict and control the thermal field during printing. Based on data collected from finite element analysis (FEA) simulations, the data-driven methods select a machine learning technique to learn the relationship between thermal field and various parameters of interest. Compared with physics-based methods, it is more

* Corresponding author.
E-mail addresses: yta88@sfu.ca (Y. Tang), mra91@sfu.ca (M. Rahmani Dehaghani), sps11@sfu.ca (P. Sajadi), shahriar.bakranibalani@tuni.fi (S.B. Balani), akshay.dhalpe@tuni.fi (A. Dhalpe), suraj.panicker@tuni.fi (S. Panicker), di.wu@tuni.fi (D. Wu), eric.coatanea@tuni.fi (E. Coatanea), gary_wang@sfu.ca (G.G. Wang).

https://doi.org/10.1016/j.jmapro.2023.11.007
Received 19 September 2023; Accepted 4 November 2023

efficient computationally and requires less knowledge about the physics behind the metal AM process. According to the parameters selected as input variables, the applications of data-driven methods could be classified as those without and those with thermal information input.

1.1. Applications without thermal information input

These applications only consider features extracted from process settings and geometries as input variables, while the thermal effects among elements in the metal AM part is not used in the modeling methods.

With 250,000 data from FEA simulations for the direct energy deposition (DED) process of stainless steel 316L, Mozaffar et al. [3] trained a recurrent neural network for thermal field prediction. In the model, the input variables were constructed as a time series structure, containing the distance-based toolpath feature, the deposition time, the distance to the part boundary, layer height, laser intensity, and laser state. After training, the mean square error of the prediction was smaller than $1e^{-4}$ for FEA simulations with different laser powers, scan speeds, toolpath strategies, and geometries. However, the part boundary would vary significantly in complex geometries, which decreases the generalization performance of some distance-based input variables.

For the DED process with a composite coating (316L and tungsten carbides), Fetni et al. [4] selected an artificial neural network to predict the thermal field from seven input features (e.g., point location, time, laser position, distance between the laser head and point, etc.). By extending the above input features with the input energy and the layer number, Pham et al. [5] utilized a feed-forward neural network for the DED process with M4 high-speed steel material powder. Both works collected training data from two-dimensional FEA simulations, and their prediction accuracies of thermal histories on selected points were over 99 %. However, their training relies on huge data sets, i.e., 4.1 million [4], and 19.9 million [5]. Moreover, as their models exclude process parameters in the input variables, both trained models cannot be applied directly to another new AM part with a different printing setting, which indicates a low generalization performance.

Based on the thermal physics, Ness et al. [6] designed eight generic features (e.g., sample time, deposition time, Euclidean distance, deposition status of adjacent nodes, power influence, etc.) for wire arc additive manufacturing (WAAM) processes with various geometries, deposition patterns and power intensities. The relationship between the designed features and the thermal field was learned by the extremely randomized tree model, which was trained by over 427,718 pieces of data collected from ABAQUS. Compared with temperature profiles from FEA simulations, the trained model provided predictions with a mean absolute percentage error below 10 % in most cases for new WAAM parts.

To identify the effects of laser scanning patterns, Ren et al. [7] proposed a deep recurrent neural network model for laser aided AM process. A two-dimensional laser deposition status matrix was designed as the input to reflect the scanning path, and the output temperature field was also represented as a matrix. After training with 47,152 pieces of data collected from FEA simulations, the model provided a prediction accuracy of over 95 % for various AM parts with any arbitrary geometry, but only parts with one single layer were discussed.

Different from the above methods relying on simulations only, Liao et al. [8] applied the physics-informed neural network (PINN) to design a hybrid physics-based data-driven thermal modeling approach for the DED process. The partial differential equation (PDE) of heat transfer was solved by the PINN model, whose training loss contained the PDE-based loss and the data-based loss, i.e., the mean square error between the prediction and the simulation/experimental data. Based on partial experimental temperature data captured by a coaxial IR camera, the trained model could predict the full temperature field of the thin wall with a root mean square error of 47.28 K, around 2.4 % of the maximum experimental temperature. However, the time-consuming training process (e.g., 100 thousand epochs in the experimental study) restricts its applicability in online updates with data measured during printing.

1.2. Applications with thermal information input

Different from the above applications, those applications with thermal information input use the temperature of adjacent elements or the temperature of previous time steps as complementary input variables, to represent the thermal transfer effect.

Paul et al. [9] proposed an iterative prediction flow based on the extremely randomized tree model, which was trained on data from time-dependent heat equations. Given one element, its temperature at one time was predicted from its temperatures during the last five time-steps, temperatures of surrounding elements at the previous time step, the relative location of the element to the laser input, and two time-related parameters. This iterative flow could predict the temperature profile of one element for the future 1000 time-steps with an R-square value of 0.969 and a relative mean absolute error below 1 %. This method is promising to be integrated into a model-based real-time AM control system, as the prediction accuracy for multiple future time steps is high. However, the computational time could be a limitation, as 68.69 s were required to predict 200 future time steps.

To consider heat transfer effects between layers in gas metal arc welding based AM, Zhou et al. [10] designed one temperature state matrix as the supplementary input for the method [7] whose input is only the deposition order state matrix. Each element in the temperature state is the average temperature value of adjacent nodes. After training with 98,585 FEA simulation data, the model could predict the thermal field of multi-layer parts with an accuracy above 94 % on the testing data. However, calculating the average temperature of one node requires the temperature of adjacent nodes on the yet-to-print layer, which are not possible to measure during the physical printing. Therefore, this method cannot be applied in actual printing for online control.

Given any arbitrary laser trajectory in the laser-based AM, Stathatos and Vosniakos [11] proposed a distance-based decomposition method to obtain the descriptor for each trajectory point. Then the temperature of one point was predicted by artificial neural networks from the point descriptor and its temperatures at previous time steps. Based on data collected from 450 FEA simulations, the trained model could predict the thermal field of various tracks (random walk, hatch pattern, etc.) with max relative errors smaller than 5 % and execution time smaller than half of the real process time. However, only a single layer was considered, and the generalization performance to multi-layer parts was not discussed.

To improve the generalizability of data-driven models in different geometries, Mozaffar et al. [12] selected the graph neural network (GNN) to capture the spatiotemporal dependencies of elements in the DED part. The thermal responses at one time step could be predicted by GNN from the thermal responses and the process parameters in the previous time step. The thermal responses for several future time steps could be estimated by the designed recurrent GNN, where the output from one time step was the input for the next time step. With the dataset generated from 50 simulated DED parts with different geometries, the trained model can predict the thermal field for a new geometry with a root mean square error smaller than 0.02.

1.3. Summary remarks

All the above data-driven modeling methods perform well on simulations, but several common limitations exist as follows:

(a) *Few considered experimental data.* Only data from FEA simulations or time-dependent heat transfer equations are chosen for training and testing, while their performances on actual metal AM printing (i.e., experiments) are seldom discussed and validated, except for [8].

(b) *Low transferability from simulation to experiments*. Different from FEA simulations and partial differential equations, the thermal behavior in actual metal AM processes is more complex as the uncertainties in process parameters and geometry deviations would affect the thermal behavior. Therefore, large prediction errors are anticipated if these models are applied to physical experiments directly.

(c) *Limited applicability in online applications*. Considering the possible unacceptable prediction performance in actual metal AM, the above models could not be applied for online applications, such as in-situ control based on predicted temperature.

Different from predicting the thermal field offline in the reviewed work, this paper aims to address the research issue for metal AM printing, i.e., *how to predict the thermal field of yet-to-print layers online with only a few temperature sensors*. To the best of the authors' knowledge, this paper is the first one that discusses this issue. As an initial exploration of potential solutions to the issue, only unidirectional printed thin walls are investigated in this paper to simplify the complexity of geometry. Specifically, when a thin wall is printed unidirectionally and a few pyrometers are used to measure the temperature profiles of points on the printed layer, this paper proposes a methodology to predict the thermal field of the yet-to-print layer online before triggering the printing of the layer.

To fulfill the purpose, two specific questions are proposed. (a) *How to map the thermal field of the printed layer to the yet-to-print layer*? When a periodic toolpath is applied to print a simple geometry or a single layer, the physical behavior on the toolpath would also be periodic to some extent, as shown in Section 2.2. Based on the periodicity, the thermal field on the yet-to-print layer could be mapped from the measured data on the printed layer. (b) *How to reconstruct the thermal field of the entire layer based on a few measured points*? In actual physical printing, high-performance thermal cameras are not always available. Often a few cheaper pyrometers are used instead to measure points of interest on a layer, which means the temperature field of the entire layer is not obtainable. Finding a method to reconstruct the thermal field of the entire layer from limited measured points would provide more feedback for prediction-based online control, which in turn reduces the reliance on high-performance sensors. By answering the above two questions, the product quality could be controlled in-situ if the relationship between a thermal field and product properties is adequately modeled.

The remainder of this paper is structured as follows. Section 2 discusses two unique characteristics of thermal behavior in metal AM, i.e., curve similarity between successive layers, and profile similarity within one layer. Section 3.1 describes the detailed settings of WAAM experiments and simulations in COMSOL Multiphysics software, as well as profile preprocessing methods. The proposed thermal field mapping and reconstruction methods are discussed in Sections 3.2 and 3.3 respectively, followed by the fine-tuning process in Section 3.4 to update the pretrained model for application to physical printing. The framework of online thermal field prediction for thin walls is then developed by combining the thermal field mapping and reconstruction. The validation, and test performances of the proposed method are shown in Section 4. Limitations of the proposed methods and their potential applications in future works are discussed in Section 5. Finally, Section 6 gives a summary of the paper.

2. Characteristics of thermal behavior

The additive and repetitive nature of a metal AM process brings about similar thermal behavior to all points in one part [13]. Moreover, the thermal behavior similarity is determined by the same fundamental physics (i.e., the continuous heat diffusion equation) followed by all points. The major difference among points is the different initial conditions caused by the thermal accumulation during printing. From the perspective of layers, the similarity could be categorized as the thermal behavior similarity within one layer and between layers, which are discussed in Sections 2.1 and 2.2 respectively. In both sections, all data are collected from a metal thin wall simulated with unidirectional printing using COMSOL Multiphysics, where a fixed travel speed is used and the dwell time is controlled to make the interpass temperature around 200 °C for each layer [2].

2.1. Temperature profiles within one layer

Fig. 1 depicts a thin wall (left most) with the temperature profiles of three points on the i-th layer under both global and local time schemes. The "*global time scheme*" is defined based on the time after the metal AM process starts working, while the "*local time scheme*" for one point is defined based on the time after the element at this point is activated.

When starting to print the i-th layer, the material is deposited to the boundary point $p_{0,i}$ and the element is activated in the simulation model. Then the temperature of $p_{0,i}$ is recorded during further printing, as shown in the temperature profile of $p_{0,i}$ in Fig. 1(a). If the time when AM process starts working is defined as 0, the global time $t_{0,i}$ when activating $p_{0,i}$ is equal to the sum of total printing time and total dwell time of all former i-1 layers. When the nozzle moves a certain distance d_j, the corresponding element at the point $p_{j,i}$ is activated at time $t_{j,i}$, after which its temperature is measured as shown in the second profile in Fig. 1(a). Considering a fixed travel speed (TS) is applied, the "*relative delay*" of the point $p_{j,i}$ on the i-th layer is defined as $t_{j,i} - t_{0,i} = d_j/TS$, which could be used to differentiate various points on the same layer. Based on this logic, all points on the i-th layer would be activated chronologically until the last boundary point $p_{end,i}$ on the layer.

After the i-th layer is printed completely, the dwell time t^i_{dwell} is applied to cool the layer down to around the required interpass temperature. Meanwhile, the temperatures of all points on the layer decrease gradually. When printing the (i+1)-th layer, the temperature at the boundary point $p_{0,i}$ on the i-th layer would increase sharply as shown as the second peak on its profile in Fig. 1(a). The reason is that its element would be re-melted or re-heated by the heat input on the next layer. But the temperatures of points on the later part of the i-th layer keep reducing, as the heat input is far from these points. With the nozzle moving, the temperature at different points would increase to the peak gradually until finishing the (i+1)-th layer. Such re-heating and re-cooling processes would repeat when printing higher layers until the entire AM part is completed.

At any global time t, the temperature field of the i-th layer consists of temperatures of all points on the layer. If the temperature profiles of all points are shifted to their local time scheme, two features could be observed from Fig. 1(b). First, the temperature trends of different profiles are similar at the same local time, while their temperature values differ. More specifically, the points on the same layer would cool down to different temperatures or re-heat to various peaks at the same local time. Second, the time duration between two successive peaks or two lowest temperatures is similar for different points. For example, the time differences from the first peak to the second peak on three temperature profiles are close for points $p_{0,i}$, $p_{j,i}$, and $p_{end,i}$, whose durations from the first peak to the first lowest value are also similar. Therefore, temperature profiles of points on the same layer have some similarities in terms of temperature trends, as well as re-heating and re-cooling durations. The similarity observed in profiles of points on the same layer is defined as "*profile similarity*" in further discussions.

2.2. Temperature profiles between layers

In this paper, the point $p_{j,i}$ on the i-th layer and the point $p_{j,i+1}$ on the (i+1)-th layer are defined as one "*point pair*" denoted as $\left(p_{j,i}, p_{j,i+1}\right)$, whose temperature profiles are shown in Fig. 2(b). Both points have the same distance d_j to the boundary point of their corresponding layer, as

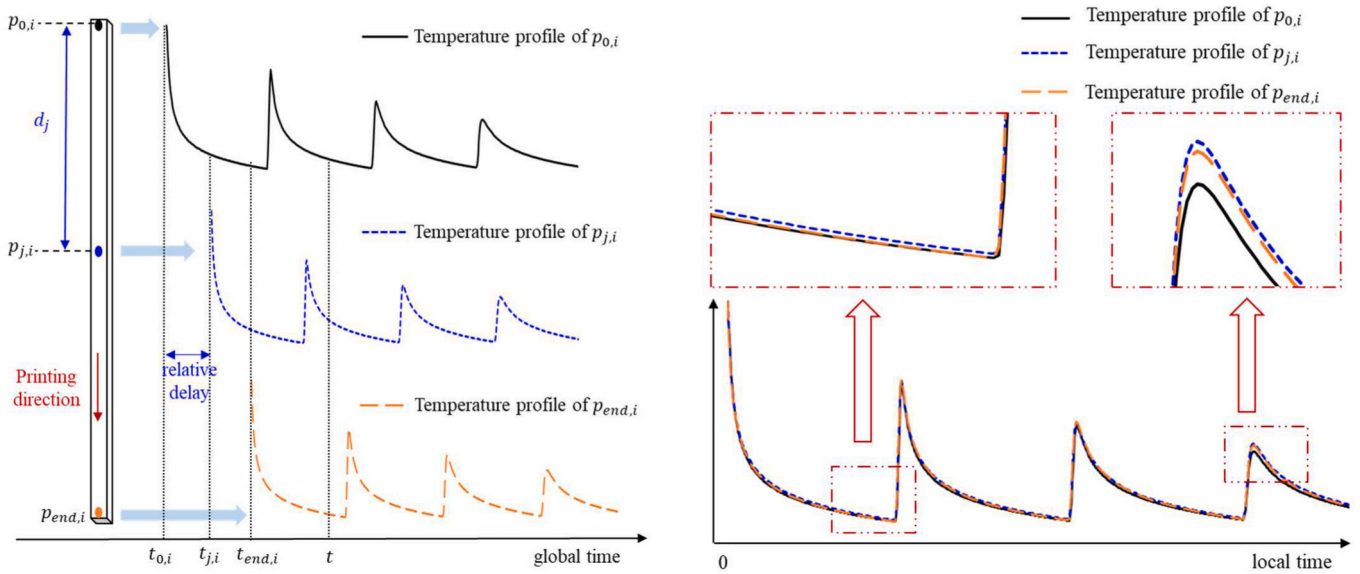

Fig. 1. Similarity of temperature profiles within the *i*-th layer.

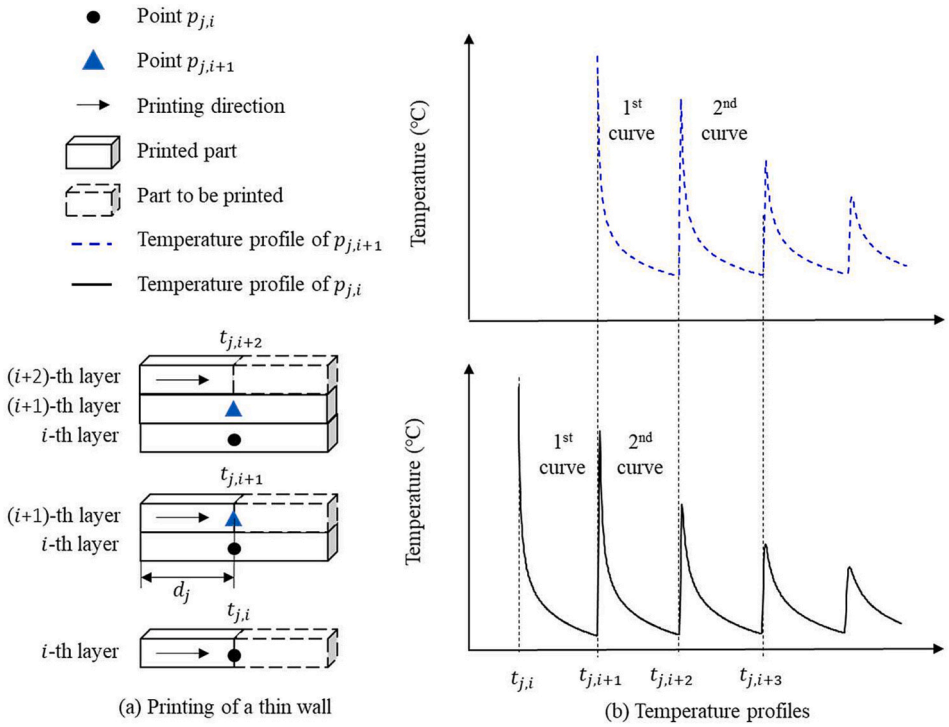

Fig. 2. Similarity of temperature profiles between layers.

shown in Fig. 2(a).

When the material is deposited to $p_{j,i}$ at $t_{j,i}$, its temperature would jump to the maximum value after which it cools down until printing the next layer. Before deposing material to $p_{j,i+1}$, the temperature at $p_{j,i}$ reduces and then increases as the heat input moves closer to the point gradually. At the time $t_{j,i+1}$, the element at the point $p_{j,i+1}$ is activated and its initial temperature is the max value. Meanwhile, the temperature at $p_{j,i}$ would increase to the peak, as the material at $p_{j,i}$ could be re-melted. From $t_{j,i+1}$ to the time $t_{j,i+2}$ when the material is deposited to the point on the (*i*+2)-th layer above $p_{j,i+1}$, the elements of $p_{j,i}$ and $p_{j,i+1}$ cool down and then are re-heated. More importantly, the temperature curve of the point $p_{j,i+1}$ during $[t_{j,i+1}, t_{j,i+2}]$ behaves similarly to the curve of the point $p_{j,i}$ during $[t_{j,i}, t_{j,i+1}]$, as shown in the first curves in Fig. 2(b). This similarity is attributed to the same phase "*activating-cooling-heating*" encountered by both points. Apart from the different initial conditions caused by heat accumulation, the major difference on both curves is the time duration. As a fixed travel speed is applied and different dwell times are applied on each layer in the simulation, $t_{j,i+1} - t_{j,i} = t_{layer} + t^{i}_{dwell}$, and $t_{j,i+2} - t_{j,i+1} = t_{layer} + t^{i+1}_{dwell}$, where t_{layer} is the time to print one layer and t^{i}_{dwell} is the dwell time for the *i*-th layer. In most cases, t^{i+1}_{dwell} is

larger than t^i_{dwell}, as more time is required for the higher layer to cool down considering the cooling rate reduces with the height [2].

Meanwhile, the curve of the point $p_{j,i+1}$ during $[t_{j,i+2}, t_{j,i+3}]$ seems similar to the curve of the point $p_{j,i}$ during $[t_{j,i+1}, t_{j,i+2}]$, as shown in the second curves in Fig. 2(b). The reason is that the point $p_{j,i}$ on the i-th layer is re-heated by the heat input on the (i+1)-th layer within $[t_{j,i+1}, t_{j,i+2}]$, and the point $p_{j,i+1}$ on the (i+1)-th layer is re-heated by the heat input on the (i+2)-th layer within $[t_{j,i+2}, t_{j,i+3}]$. For both points, the layer distance between the point layer and the heat-input layer is identical. This phenomenon is also applicable to any other two curves with the same index number.

Therefore, given any point pair $\left(p_{j,i}, p_{j,i+1}\right)$, the k-th curve $\boldsymbol{C}^k_{j,i}$ in the temperature profile of $p_{j,i}$ is always similar to the k-th curve $\boldsymbol{C}^k_{j,i+1}$ in the temperature profile of $p_{j,i+1}$ considering the similar re-heating-cooling cycle encountered by both points. For clarification, this similarity between two successive layers is defined as "*curve similarity*", and $\left(\boldsymbol{C}^k_{j,i}, \boldsymbol{C}^k_{j,i+1}\right)$ is defined as a "*curve pair*" containing such similarity.

2.3. Summary remarks

Both analyses are based on a thin wall with the same process setting on each layer, which means the printing direction, the travel speed, the wire feed rate, and other process parameters are fixed during the printing. Therefore, the time to print one layer is fixed for all layers. And the duration from depositing the material to re-heating the same point is identical for any points on the same layer. Although similarities in such a thin wall could be observed easily in the simulated temperature profiles, the thermal behavior in actual experiments is more complex considering the uncertainties in various factors, such as the printing process, material property, and geometry deviations. In this paper, several assumptions are applied as follows to simplify the effects of differences between simulations and actual experiments on modeling processes.

(a) *Constant Power*: In WAAM experiments, the metal wire is heated by the electric arc whose current I and voltage V change during the printing process. Although the dynamic update of current and voltage happens internally in the algorithm of the CMT Fronius apparatus, they are not captured in the FEA simulations. Therefore, in one single simulation or experiment, the power $P = I \bullet V$ is assumed as constant during printing.
(b) *Constant Process Parameters*. During the printing process, the predefined process parameters, i.e., travel speed and wire feed rate, would change dynamically. These dynamic changes are not set in simulations. For simplification, once being set, the process parameters are assumed to be constant in both simulations and experiments.
(c) *Fixed Layer Thickness*: The layer thickness is set as a constant in FEA simulations, but the value varies in actual WAAM experiments considering the effects of geometry deviations. Specifically, although a constant step height is applied in the experiment, the thicknesses of printed layers are different and not equal to the step height. For simplification, the layer thickness in one experiment is assumed to be the same as the step height during the online prediction.
(d) *No Effect of Geometry Deviation*: The geometry deviation could affect the thermal behavior significantly during actual experiments, but they are only measured after the part is completed. In other words, the geometry deviation could not be an input variable for the online control. Therefore, the geometry deviation is assumed to not affect the profile similarities and curve similarities.

3. Methods

3.1. Data preparation

Several simulations and WAAM experiments are completed for thin walls with unidirectional printing to collect temperature profiles by corresponding preprocessing methods for further discussion and testing.

3.1.1. Experimental setup

Based on the same machine system in the work [2], the experimental thermal data are collected from cold metal transfer based WAAM (CMT-WAAM) experiments, whose detailed setup is discussed in our previous work [14]. The travel speed *TS*, the wire feed rate *WFR*, and the shielding gas flow rate *SGFR* are chosen as the process parameters to design several experiments, as they are the most effective parameters in the CMT-WAAM process [15]. Each parameter has three levels, i.e., $TS \in \{8, 11, 15\}$, $WFR \in \{3, 4.5, 6\}$, and $SGFR \in \{12, 16, 20\}$, to cover the WFR/TS range [3.33,12.5] in the study [2] and the *SGFR* values used in other CMT-WAAM studies [16–18]. In this paper, the central composite faced design of experiment is applied to generate 15 experiments, whose details are shown in Table 1.

In each experiment, a thin wall with a fixed length 160 mm is printed with the AM70 alloy steel wire [19], whose diameter is 1.2 mm. Then the deposition rate, *DR*, is calculated as $3.14 \times 0.6^2 \times WFR \times 1000/60$. The baseplate is an S355 mild steel plate [20] with size 300 mm × 50 mm × 20 mm. The chemical compositions of AM70 and S355 are summarized in Table 2. The step height *SH* is set manually to make sure a successful printing of each wall, based on which the relative height of the i-th layer is estimated as $h_i = i \times SH$. The time to print one layer t_{layer} is extracted from the ABB robot event log files. All these values are shown in Table 1.

During the printing, the dwell time is applied to make sure the interpass temperature is around 200 °C. The dwell time t^i_{dwell} of the i-th layer is estimated as the difference between the absolute time from starting printing the i-th layer to starting printing the (i+1)-th layer and the calculated printing time t_{layer}. Due to the limited equipment, the temperature of the middle point on the side of the layer is detected every five layers. More specifically, the pyrometer is set to measure the temperature of the middle point on the first layer when printing the first layer to the fifth layer, to guarantee five temperature curves in each profile. When starting to print the sixth layer, the pyrometer is moved to record the temperature of the middle point on the sixth layer before printing the eleventh layer. Therefore, the point pair in experiments is defined as the middle points on the i-th layer and (i+5)-th layer, such as the first layer and the sixth layer. Considering the measurement capability of the applied pyrometer, the temperature above 1000 °C and the temperature below 150 °C would be truncated to the corresponding boundary as shown in Fig. 3, which cannot reflect the actual

Table 1
Details of 15 CMT-WAAM experiments.

Experiment no.	*TS* (mm/s)	*WFR* (m/min)	*SGFR* (L/min)	*SH* (mm)	t_{layer} (s)	*DR* (mm³/s)
1	8	3	12	1.6	20.2	56.52
2	8	6	20	1.6	20.2	113.04
3	8	6	12	2	20.2	113.04
4	8	3	20	2	20.2	56.52
5	15	3	20	1.4	10.9	56.52
6	15	3	12	1.4	10.9	56.52
7	15	6	12	1.6	10.9	113.04
8	15	6	20	1.6	10.9	113.04
9	11	4.5	16	1.5	14.8	84.78
10	8	4.5	16	1.8	20.2	84.78
11	15	4.5	16	1.5	10.9	84.78
12	11	3	16	1.5	14.8	56.52
13	11	6	16	1.8	14.8	113.04
14	11	4.5	12	1.6	14.8	84.78
15	11	4.5	20	1.7	14.8	84.78

Table 2
Chemical compositions in percentage by weight (wt%) of AM70 and S355.

Material	Element (wt%)					
AM70 [19]	C	Si	Mn	Cr	Mo	Ni
	0.08	0.60	1.70	0.20	0.50	1.50
S355 [20]	C	Si	Mn	P	S	
	≤0.20	≤0.55	≤1.60	≤0.035	≤0.035	

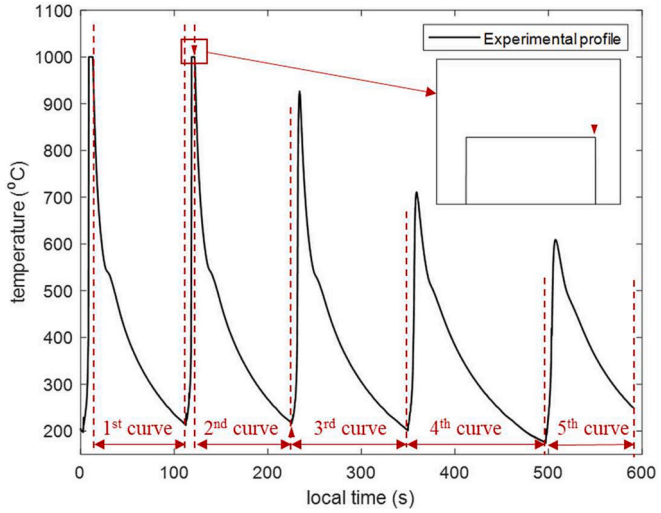

Fig. 3. Temperature profile recorded by pyrometer.

temperature profile. In this paper, only experimental curves below 1000 °C are considered.

Different from the profile preprocessing for simulations in Section 3.1.2, the experimental temperature profile is split at each temperature sharp rise on the profile, shown as the red dashed line in Fig. 3. The reason is that the exact locations of measured points are not accessible during experiments, which is attributed to the deviations caused by moving the pyrometer manually. In theory, such a split method has minor effects on testing the proposed prediction method. One point of the work is to learn the curve similarity by the thermal field mapping, while this similarity is also observed among the obtained experimental temperature curves. Finally, 29 point-pairs and 145 curve-pairs are obtained from the experiments.

3.1.2. Simulation setup

The COMSOL Multiphysics software is applied to simulate the CMT-WAAM process under the assumptions in Section 2.3, e.g., the power, process parameters and layer thickness keep constant in one simulation, and no geometry deviation exists. As the shielding gas is not applicable in the software, the travel speed (TS) and the wire feed rate (WFR) from completed experiments are selected to design nine simulations, as shown in Table 4. The materials in simulations are identical to experiments, i.e., S355 mild steel for the baseplate with a fixed geometry size 300 mm × 200 mm × 20 mm, and AM70 alloy steel for the part. The physical properties of materials applied in the simulations are summarized in Table 3.

In each simulation, a thin wall with a layer width 4.4 mm, a layer length 160 mm, and 40 layers is studied. The layer thickness l_t is set according to step heights applied in actual WAAM experiments. Then the relative height of the i-th layer is calculated as $h_i = i \times l_t$. The deposition rate DR is estimated as $4.4 \times l_t \times TS$ for the simulation. The printing time t_{layer} for one layer is set as $160/TS + 0.5$, where 0.5 is a constant total estimation of the acceleration time at the starting point and the deceleration time at the ending point of one layer. For each layer, a dwell time is set manually to make sure that the temperature of points on the layer could decrease to around 200 °C, after which the deposition of the next layer is triggered. Meanwhile, a constant energy E is applied in the simulation for melting, which is defined as,

$$E = Pe \times I \times V / V_b \tag{1}$$

where Pe is the process efficiency 0.85, and $V_b = 4.4 \times 160 \times l_t$ is the bead volume. The current I and the voltage V are determined as functions of WFR based on experimental studies, i.e., $I = 1.22 \times WFR + 5.2444$, and $V = 27.267 \times WFR + 10.556$. Finally, the segregated study with the MUMPS direct solver is used for the numerical simulations; detailed equations could be found in [21].

To collect sufficient temperature profiles, seven points are set evenly on the side of each layer, as shown in Fig. 4. According to the printing direction, the point $p_{j,i}, j \in [1,7]$ is located with a distance $20j$ mm to the starting point of the i-th layer. Therefore, seven point-pairs could be generated among every two successive layers in the simulation.

For the temperature profile of any point $p_{j,i}$ in the thin wall, it encounters multiple "*re-heating-cooling*" cycles according to the printing and cooling on higher layers, as shown in Fig. 5. Given the travel speed TS, the printing time t_{layer} of one layer, the dwell time t^i_{dwell} of each i-th layer, and the distance d_j between $p_{j,i}$ and the boundary point $p_{0,i}$, the global time $t_{j,i}$ when the material is deposited to $p_{j,i}$ could be estimated offline or online as follows.

$$t_{j,i} = (i-1)t_{layer} + \sum_{m=1}^{i-1} t^m_{dwell} + d_j \Big/ TS \tag{2}$$

Based on the thermal behavior discussed in Section 2, the temperature profile could be split into several curves according to the estimated time series $\{t_{j,i}, t_{j,i+1}, t_{j,i+2}, \ldots\}$ as shown in Fig. 5. For clarification, the partial profile within $[t_{j,i+k-1}, t_{j,i+k}]$ is defined as the k-th temperature curve of the point $p_{j,i}$, whose duration is a fixed value for all points on the same layer, i.e., $t_{j,i+k} - t_{j,i+k-1} = t_{layer} + t^{i+k-1}_{dwell}$. This phenomenon has also been observed in Section 2.1. However, a short-term increase could be observed in the tail of each raw curve, as shown in the red circles in Fig. 5. This reason is that the element at one point would be re-heated when the distance between the heat input on the higher layer and the point is smaller than a certain value in the FEA simulation, as well as the effect of heat transfer. For simplification, this short-term increase will not be considered in the online prediction method in Section 3.5, as its duration is negligible compared to the entire duration of one curve. Therefore, the smoothed curves after processing are selected for further application in the paper.

Besides, the durations of all temperature curves at one point are different, as the dwell time increases with the layer, i.e., $t^{i+1}_{dwell} \geq t^i_{dwell}$. To represent these temperature curves with various durations, a fixed number N of discrete temperature data is sampled evenly from each curve. Therefore, the k-th temperature curve $\boldsymbol{C}^k_{j,i}$ of point $p_{j,i}$ could be

Table 3
Physical properties applied in the simulation.

Physical property	AM70 [19]	S355 [20]
Density (g/cm^3)	8.3	7.8
Thermal conductivity (W/(m·K))	19	42.5
Specific heat capacity (J/(kg·K))	460	470

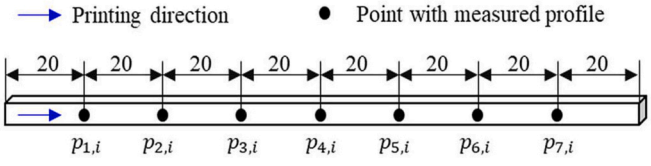

Fig. 4. Points located on the i-th layer in simulations.

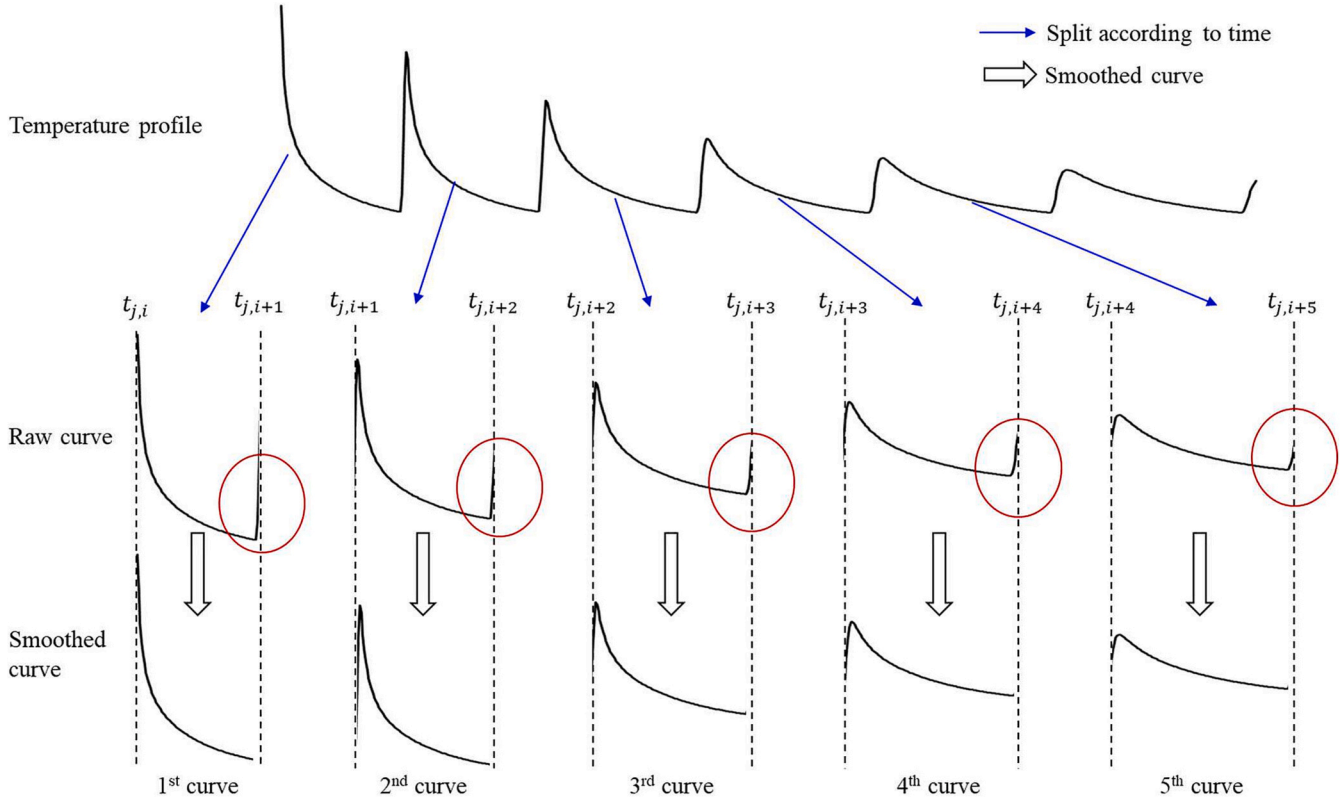

Fig. 5. Temperature profile vs temperature curves.

formulated as $\boldsymbol{C}_{j,i}^{k} = \left[T_{j,i}^{k,1}, \ldots T_{j,i}^{k,n}, \ldots, T_{j,i}^{k,N}\right]$, where $T_{j,i}^{k,n}$ is the n-th sampled temperature data.

Theoretically, as the remaining number of layers decreases as the geometry is built, the number of re-heating cycles is reduced. Hence, the number of temperature curves decreases with the increase of layers. In this paper, for consistency only the first five curves, also the most influential curves, on the temperature profile of every point are selected for discussion. As a result, the temperature profile $\boldsymbol{P}_{j,i}$ of point $p_{j,i}$ is represented as $\boldsymbol{P}_{j,i} = \left[\boldsymbol{C}_{j,i}^{1}, \boldsymbol{C}_{j,i}^{2}, \boldsymbol{C}_{j,i}^{3}, \boldsymbol{C}_{j,i}^{4}, \boldsymbol{C}_{j,i}^{5}\right]$.

Based on the above profile processing, the collected temperature profiles from one simulation can generate 1260 curve pairs in total, which means 11,340 curve pairs from all nine simulations.

3.1.3. Comparison

As this paper considers the practical scenario where only a few sensors are available and the temperature of points inside the part is not accessible during printing, only the temperatures of points on the surface are considered. To quantify the difference between the completed experiments and simulations, the side view of one fabricated thin wall with unidirectional printing is shown in Fig. 6(a). Different from geometries in simulations, rough surfaces and geometry deviations are observed in all experiments. Meanwhile, Fig. 6(b) shows the temperature profiles of the middle point on the 21th layer from an experiment and a simulation, both holding the same *TS* and *WFR*. Although the interpass temperatures from the experiment and simulation are similar, the recorded maximum temperature and the dwell time required to cool down to around 200 °C are quite different. These differences are attributed to several factors, i.e., (a) various sizes of the base plate in simulations and experiments, (b) excluding effects of shielding gas and

(a) One printed thin wall

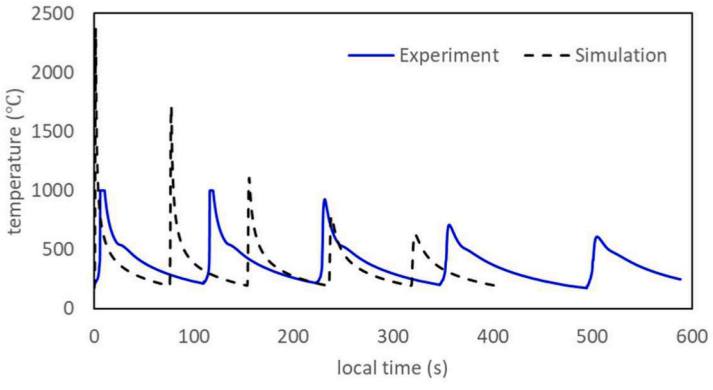

(b) Temperature profiles

Fig. 6. Comparison between temperature profiles from simulation and experiment.

geometry deviation on heat transfer in simulations, and (c) limited sensor capability for the truncated experimental temperature profile. Therefore, the designed simulation cannot capture the physical experiments exactly and accurately.

As the purpose of the simulation is to provide data for model training and validation, we will show these differences, however, would not deteriorate the generalization performance of the proposed methods in Sections 3.2 and 3.3. Even though the model is only pretrained with simulation data, the proposed method still shows a great generalization capability for the actual experiments when the model is fine-tuned with limited experimental data, as discussed in Section 4.1.3.

3.2. Thermal field mapping

In metal AM, the periodic toolpath would be adopted to print some simple geometries (i.e., thin walls) or a single layer. As all points on the toolpath follow the same physical law while the only difference is the initial condition, the thermal field of these points would be periodic, just as the curve similarity in Section 2.2. Based on the observed similarity, the thermal field of points on the printed part could be mapped to the points on the yet-to-print part. This mapping is close to the reviewed data-driven modeling methods with thermal information input in Section 1.2. The major difference is that the proposed mapping aims to predict the thermal field of the yet-to-print part from printed parts, while the reviewed works [9,11,12] focus on predicting the temperature of printed parts at one timestep based on the thermal information from previous timesteps. The methodology of the proposed thermal field mapping is discussed as follows based on the unidirectionally printed thin wall.

3.2.1. Modeling objective

For the thin wall with unidirectional printing, based on the discussion in Section 2.2, given the k-th temperature curve $\boldsymbol{C}_{j,i}^{k}$ of the point $p_{j,i}$ on the i-th layer, the counterpart one with similarity is the k-th temperature curve $\boldsymbol{C}_{j,i+1}^{k}$ of the point $p_{j,i+1}$ on the (i+1)-th layer. That means the point pair on the successive layer is selected for the thermal field mapping. If the curve similarity is formulated as a model $f_{mapping}(\cdot)$, the curve $\boldsymbol{C}_{j,i+1}^{k}$ could be represented as a function $\boldsymbol{C}_{j,i+1}^{k} = f_{mapping}\left(\boldsymbol{C}_{j,i}^{k}, \boldsymbol{x}_{mapping}\right)$, where $\boldsymbol{x}_{mapping}$ contains other input variables. However, as $dt_i \le dt_{i+1}$, the duration of the curve $\boldsymbol{C}_{j,i}^{k}$, i.e., $t_{layer} + t_{dwell}^{i+k-1}$, is smaller than the duration of the curve $\boldsymbol{C}_{j,i+1}^{k}$, i.e., $t_{layer} + t_{dwell}^{i+k}$. In other words, the length of the curve $\boldsymbol{C}_{j,i}^{k}$ is shorter than the curve $\boldsymbol{C}_{j,i+1}^{k}$ as shown in Fig. 7, where the starting time of each curve is defined as the local time 0. To maintain the curve similarity when training $f_{mapping}(\cdot)$, only the partial curve $\boldsymbol{C}_{j,i+1}^{k'}$ within the overlapped duration on $\boldsymbol{C}_{j,i+1}^{k}$ is defined as the output of the model, i.e., $\boldsymbol{C}_{j,i+1}^{k'} = f_{mapping}\left(\boldsymbol{C}_{j,i}^{k}, \boldsymbol{x}_{mapping}\right)$. In this paper, both $\boldsymbol{C}_{j,i+1}^{k'}$ and $\boldsymbol{C}_{j,i+1}^{k}$ are represented as an $1 \times N$ vector with different sampling periods as discussed in Section 3.1.2.

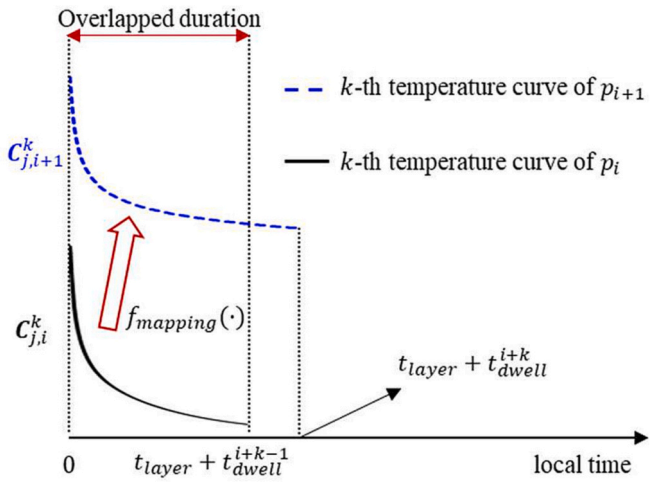

Fig. 7. Illustration of k-th curves of a point pair under local time.

According to [13], each temperature curve follows an exponential formulation, which is attributed to the exponential re-heating and cooling behavior. This indicates that the predicted partial curve $\boldsymbol{C}_{j,i+1}^{k'}$ could be used to extrapolate the entire curve $\boldsymbol{C}_{j,i+1}^{k}$ based on the local time, which provides a possibility to predict the dwell time of the yet-to-print layer to cool down to the required interpass temperature. Finding the global optimal modeling method, however, is not the purpose of the paper, the extrapolation from $\boldsymbol{C}_{j,i+1}^{k'}$ to $\boldsymbol{C}_{j,i+1}^{k}$ will not be considered in the following sections for simplification. Therefore, the profile of the point on the yet-to-print layer is only represented with partial curves in this work, i.e., $\boldsymbol{P}_{j,i} = \left[\boldsymbol{C}_{j,i}^{1'}, \boldsymbol{C}_{j,i}^{2'}, \boldsymbol{C}_{j,i}^{3'}, \boldsymbol{C}_{j,i}^{4'}, \boldsymbol{C}_{j,i}^{5'}\right]$.

3.2.2. Input variables

In the thermal field mapping, some complementary input variables need to be considered that affect the similarities between the points on the printed and yet-to-print layers, as well as those features affecting the heat transfer. These input variables could include the distance (i.e., distance of points to the cooling surfaces and heat sources [13]), the heat input (i.e., heat influence zone [13], power influence [6]), the toolpath (i.e., deposition time of one node [6]), and so on.

As this paper only studies the simple geometry and toolpath, i.e., thin wall with unidirectional printing, four features are selected as the complementary input variables to improve the generalization of $f_{mapping}(\cdot)$ in various applications (e.g., online/offline prediction of thin walls with different process settings), i.e., $\boldsymbol{x}_{mapping} = \left[t_{layer}, t_{dwell}^{i}, DR, h_i\right]$. For more complex geometries and toolpaths, more input variables should be considered accordingly, which is not covered in this paper.

(a) *Printing time of one layer*, t_{layer} (unit: s): The heat input in WAAM experiments is the energy per unit length, which is formulated as P/TS with the unit J/mm [22]. Given the length of one layer L (mm), the total heat input on the layer is formulated as $P \bullet L/TS$. As the power P is assumed as a constant in this paper and the modeling purpose of $f_{mapping}(\cdot)$ is to learn the curve similarity, the effect of heat input on the curve could be simplified and reflected by the time to print one layer, i.e., $t_{layer} = L/TS$.

(b) *Dwell time of the i-th layer*, t_{dwell}^{i} (unit: s): When one layer in the thin wall is printed completely, the dwell time is taken until the interpass temperature cools down to the required value. Although the cooling rate during this process depends on several factors (e.g., the time, the radiation/convection coefficient, and the external cooling system), only the dwell time is selected as the variable to indicate the effect of cooling rate on the temperature curve in this paper.

(c) *Deposition rate*, DR (unit: mm^3/s): In actual WAAM experiments, the deposition rate could be estimated as $DR = \pi \times (d/2)^2 \times WFR \times 1000/60$, where d (mm) is the diameter of the metal wire, and WFR (m/*min*) is the wire feed rate in the process. Therefore, the volume of one printed layer is estimated as the product of the printing time and the deposition rate. Moreover, as a larger WFR value indicates a higher input [23], the deposition rate could be a general variable to reflect the total heat input in one layer when metal wires of various diameters are used.

(d) *Relative height of the i-th layer*, h_i (unit: mm): In WAAM processes, the difference in the initial thermal conditions to print each layer decreases with the height. More specifically, the initial thermal condition to print the first layer is related to the substrate only, while

the initial condition for the second layer depends on the thermal field of the first layer. As a certain interpass temperature is maintained during printing, the difference between the initial thermal conditions of the first and the second layers would be larger than the differences between the second and the third layer. One reflection of the difference reduction is that the cooling rate would decrease gradually to a stable value with height. Another reflection is the increasing curve similarity, which means the difference between the k-th curves of a point pair $\left(p_{j,i}, p_{j,i+1}\right)$ decreases with height, as shown in Fig. 8. The input curve refers to the temperature curve of the point on the lower layer, while the output one is the curve of the point on the higher layer. To reflect the effect of the height in the model $f_{mapping}(\cdot)$, the relative height h_i of the i-th layer to the substrate is defined as one input variable, i.e., $h_i = i \bullet l_t$, where l_t is the constant layer thickness.

3.2.3. Model structure

Based on the above discussions, the thermal field mapping model is finally formulated as $\boldsymbol{C}_{j,i+1}^{k'} = f_{mapping}\left(\boldsymbol{C}_{j,i}^{k}, t_{layer}, t_{dwell}^{i}, DR, h_i\right)$, which has $N + 4$ input variables and N outputs. This means the proposed mapping model is a multi-input-multi-output (MIMO) regression task. In this paper, the artificial neural network is chosen to construct the model $f_{mapping}(\cdot)$, considering its ability to process noisy data (i.e., the experimental temperature data), easy implementation, and vast successful applications in different MIMO tasks, such as nonlinear control systems [24], image segmentation [25], and transportation [26].

Theoretically, an optimal neural network exists for the thermal field mapping model $f_{mapping}(\cdot)$ to receive the best performance. Generally, an optimization problem is solved to find optimal hyperparameters of the neural network, including the number of hidden layers, the number of hidden neurons on each layer, the activating function for each hidden layer, the learning rate, the epoch number for training, and other model structure parameters. This is the topic of "*hyperparameter optimization*" in deep learning [27], which is not covered in this paper, however.

Instead of solving a hyperparameter optimization problem, a fully connected network with residual connection (FCN-RC) is selected as $f_{mapping}(\cdot)$ after several trials, as it provides acceptable testing performance for this problem. The model structure is shown in Fig. 9. A linear connection layer Linear(·) and the activation function ReLu(·) are chosen for each hidden layer. As the size of elements in $\boldsymbol{C}_{j,i}^{k}$ could be set as various values, the number of hidden nodes on each layer is defined according to N, i.e., $3N$, $6N$, $12N$, $6N$, $3N$, N nodes are set from the first to the sixth hidden layer respectively. In theory, there are total $186N^2 + 35N$ parameters for learning in the model. A dropout layer with a rate 0.1 is applied before the output layer to reduce the risk of overfitting. Then a residual connection is used to combine the input curve $\boldsymbol{C}_{j,i}^{k}$ to form the final output, i.e., $\boldsymbol{C}_{j,i+1}^{k'} = FCN\left(\boldsymbol{C}_{j,i}^{k}, t_{layer}, t_{dwell}^{i}, DR, h_i\right) + \boldsymbol{C}_{j,i}^{k}$. Given the number of training epoch, the residual connection could make the training easier and improve learning performance [28]. During training, the Adam optimizer [29] is applied with the mean square error loss, with the initial learning rate 0.001 and the total training epoch number 500. Besides, the learning rate is reduced by a ratio of 0.5 after every 100 epochs to improve the convergence. Based on above setups, the detailed training process of the proposed thermal field mapping model $f_{mapping}(\cdot)$ is shown in Table 5. In this paper, all codes are implemented based on Pytorch [30].

3.3. Thermal field reconstruction

Different from the thermal field mapping designed for similar temperature curves, the thermal field reconstruction aims to predict the thermal field of the entire layer based on several measured points, which does not rely on the similarity observed in Section 2.

3.3.1. Modeling objective

In the thermal field reconstruction, only temperature profiles of points on the same layer are considered. For instance, discrete points are located on the i-th layer, denoted as $p_{j,i}, j \in [1, M]$, where M is the total number of measured points on the layer. As mentioned in Section 2.1, some factors $\boldsymbol{x}_{recons}$ could be used to differentiate points on the same layer, i.e., $p_{j,i} \sim \boldsymbol{x}_{recons}^{j}$. Then the relationship between $\boldsymbol{x}_{recons}^{j}$ and the corresponding temperature profile $\boldsymbol{P}_{j,i}$ could be modeled as a function, i.e., $\boldsymbol{P}_{j,i} = f_{recons}\left(\boldsymbol{x}_{recons}^{j}\right)$, where $f_{recons}(\cdot)$ is the thermal field reconstruction model. When given an unseen point p' whose factor is $\boldsymbol{x}_{recons}^{'}$, its temperature profile $\boldsymbol{P}'$ could be estimated as $\boldsymbol{P}' = f_{recons}\left(\boldsymbol{x}_{recons}^{'}\right)$ directly.

3.3.2. Input variables

Generally, the factors $\boldsymbol{x}_{recons}$ of one point could be designed based on the toolpath on the layer, i.e., the deposition time (relative delay), and the relative distance to the starting point. In this paper, only the relative delay $t_{rd}^{j} = d_j / TS$ of point $p_{j,i}$ is selected as $\boldsymbol{x}_{recons}^{j}$ to differentiate points on the same layer in the thin wall, where d_j is the distance to the boundary point of the layer and TS is the travel speed. Then the thermal field reconstruction model could be simplified as $\boldsymbol{P}' = f_{recons}\left(t_{rd}^{'}\right)$ and $\boldsymbol{P}_{j,i} = f_{recons}\left(t_{rd}^{j}\right)$.

3.3.3. Model structure

For the thin wall discussed in Section 3.1, each temperature profile is constructed with five predicted curves, whose dimension is then $1 \times 5N$. Therefore, the training of the thermal field reconstruction model $f_{recons}(\cdot)$ is a single-input-multi-output regression task. To keep the accuracy of the curve representation $\boldsymbol{C}_{j,i}^{k}$, the size N of temperature data sampled on each curve is set as a large value, then the size $5N$ would be in hundreds or thousands. However, considering the limitation of sensors and the constraints of geometry size, M is in tens (also the training data size), which means $5N$ is much larger than M in actual experiments. In this case, the training performance of the high-dimension-output model would be poor; and the overfitting problem would exist and the generalization performance is worse on testing data.

To decrease the huge diversity between the training data size and the output size, the non-intrusive reduced order model (ROM) method is applied for dimension reduction in this paper. It is a kind of technology to decompose the responses of complex systems with a high degree of freedom into low-dimensional intrinsic features [31]. For example, given a bunch of responses (snapshots) from the same system with various boundary conditions, multiple common features could be extracted from the response matrix by model decomposition methods, such as the proper orthogonal decomposition (POD) [32]. Then each snapshot could be represented as a combination of all common features, where the feature coefficients are modeled as a function of the boundary conditions. When the raw snapshots are decomposed directly without any nonlinear preprocessing, the obtained common features are linear combinations of snapshots with various coefficients. Therefore, the final ROM solution for a new boundary condition is also a linear combination of snapshots. Generally, the accuracy of the ROM solution increases with the linearity observed [32]. Due to the efficiency and accuracy of ROM methods in constructing and representing high-dimensional responses, the non-intrusive ROM method has been applied widely in various engineering problems, such as heat transfer for unsteady flow [33], natural convection in porous media [34], and structure responses [35].

3.3.3.1. Profile decomposition by POD. Based on the profiles $\boldsymbol{P}_{j,i}$ of all point $p_{j,i}$ ($j \in [1, M]$) on the i-th layer, a profile matrix $\boldsymbol{S}$ is defined as $\boldsymbol{S} = \left[\boldsymbol{P}_{1,i}^{T}, \ldots, \boldsymbol{P}_{j,i}^{T}, \ldots, \boldsymbol{P}_{M,i}^{T}\right]$ with the size $5N \times M$, where $5N \gg M$, and $\boldsymbol{P}_{j,i}^{T}$ is the transposition of the profile vector $\boldsymbol{P}_{j,i}$. Then the singular value decomposition of the profile matrix is conducted as:

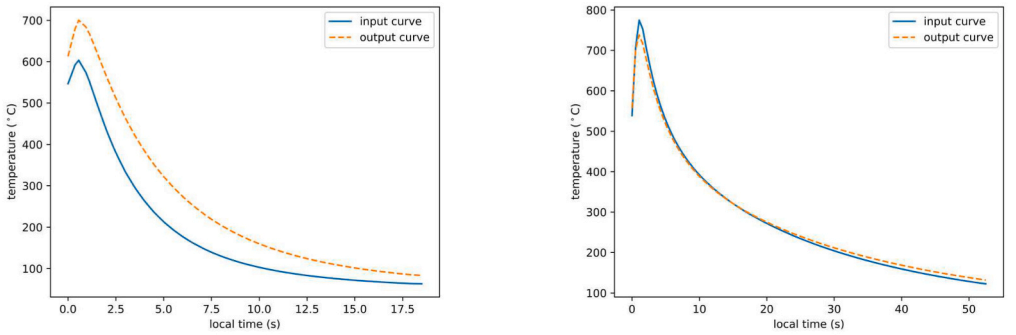

(a) Curve of the point pair on the 1st and 2nd layer (b) Curve of the point pair on the 10th and 11th layer

Fig. 8. Similarity between the third curves of point pairs.

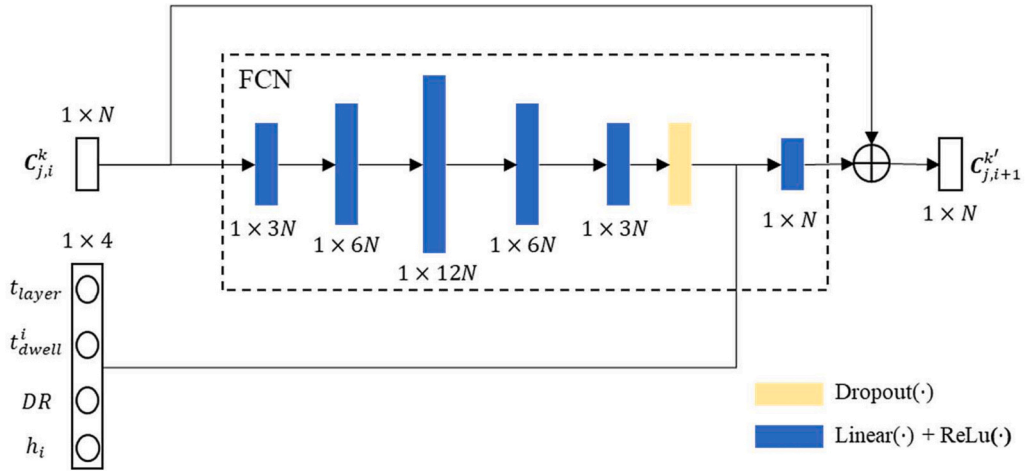

Fig. 9. Structure of the thermal field mapping model $f_{mapping}(\cdot)$.

$$\boldsymbol{S} = \boldsymbol{U}\boldsymbol{\Sigma}\boldsymbol{V}^T = [\boldsymbol{u}_1, \ldots, \boldsymbol{u}_{5N}]_{5N\times 5N} \begin{bmatrix} \lambda_1 & 0 & 0 \\ 0 & \ldots & 0 \\ 0 & 0 & \lambda_M \\ & \boldsymbol{0} & \end{bmatrix}_{5N\times M} [\boldsymbol{v}_1, \ldots, \boldsymbol{v}_M]_{M\times M} \tag{3}$$

where $\boldsymbol{u}_1, \ldots, \boldsymbol{u}_{5N}$ are the left singular vectors, $\boldsymbol{v}_1, \ldots, \boldsymbol{v}_M$ are the right singular vectors, and $\lambda_1, \ldots, \lambda_M$ are the singular values with the relationship $\lambda_1 \geq \lambda_2 \geq \ldots \geq \lambda_M \geq 0$. As $\boldsymbol{0}$ is a zero matrix with size $(5N - M) \times M$, the above equation could be simplified as follow.

$$\boldsymbol{S} = [\boldsymbol{u}_1, \ldots, \boldsymbol{u}_M]_{5N\times M} \begin{bmatrix} \lambda_1 & 0 & 0 \\ 0 & \ldots & 0 \\ 0 & 0 & \lambda_M \end{bmatrix}_{M\times M} [\boldsymbol{v}_1, \ldots, \boldsymbol{v}_M]_{M\times M} \tag{4}$$

A coefficient matrix is defined as $\boldsymbol{C} = diag(\lambda_1, \ldots, \lambda_M)[\boldsymbol{v}_1, \ldots, \boldsymbol{v}_M] = [\boldsymbol{C}_1, \ldots, \boldsymbol{C}_M]$, where $\boldsymbol{C}_1, \ldots, \boldsymbol{C}_M$ are the coefficient vectors with an identical size $M \times 1$. Then, the formulation in Eq. (4) is rewritten as:

$$\boldsymbol{S} = [\boldsymbol{u}_1, \ldots, \boldsymbol{u}_M]_{5N\times M}[\boldsymbol{C}_1, \ldots, \boldsymbol{C}_M]_{M\times M} = \left[\boldsymbol{P}_{1,i}^T, \ldots, \boldsymbol{P}_{j,i}^T, \ldots, \boldsymbol{P}_{M,i}^T\right] \tag{5}$$

Therefore, each temperature profile $\boldsymbol{P}_{j,i}^T$ could be calculated as:

$$\boldsymbol{P}_{j,i}^T = [\boldsymbol{u}_1, \ldots, \boldsymbol{u}_M]_{5N\times M}\left[\boldsymbol{C}_j\right]_{M\times 1} = \sum_{m=1}^{M} \boldsymbol{u}_m c_j^m \tag{6}$$

In the field of ROM, $\boldsymbol{u}_1, \ldots, \boldsymbol{u}_M$ are defined as the reduced bases, which are identical for each column in the matrix $\boldsymbol{S}$. To find the minimum number M^* of the required reduced bases while maintaining the accuracy of the final solution, the energy percentage ε defined based on the singular value is used as the criteria [36].

$$\varepsilon = \frac{\sum_{m=1}^{M^*} \lambda_m^2}{\sum_{m=1}^{M} \lambda_m^2} \geq 99\% \tag{7}$$

After obtaining the optimal number, the former M^* reduced bases (left singular vectors) and their corresponding coefficients in Eq. (6) are selected to reformulate the $\boldsymbol{P}_{j,i}^T$ as the following equation:

$$\boldsymbol{P}_{j,i}^T \approx \widehat{\boldsymbol{U}}\widehat{\boldsymbol{C}}_j = [\boldsymbol{u}_1, \ldots, \boldsymbol{u}_{M^*}]_{5N\times M^*}\left[c_j^1, \ldots, c_j^{M^*}\right]^T = \sum_{m=1}^{M^*} \boldsymbol{u}_m c_j^m \tag{8}$$

where $\widehat{\boldsymbol{U}} = [\boldsymbol{u}_1, \ldots, \boldsymbol{u}_{M^*}]_{5N\times M^*}$ is the reduced basis matrix with selected bases, and $\widehat{\boldsymbol{C}}_j$ contains the basis coefficients of the point $p_{j,i}$.

3.3.3.2. Profile construction by ELM. After decomposing the profile matrix $\boldsymbol{S}$ of the i-th layer, the profile $\boldsymbol{P}_{j,i}$ of the point $p_{j,i}$ only depends on the basis coefficients $\widehat{\boldsymbol{C}}_j$, while the reduced bases $\boldsymbol{u}_1, \ldots, \boldsymbol{u}_{M^*}$ are identical for all points on the same layer. Therefore, the relationship between the relative delay t_{rd}^j and the profile $\boldsymbol{P}_{j,i}$, i.e., $\boldsymbol{P}_{j,i} = f_{recons}\left(t_{rd}^j\right)$, could be simplified as the one between t_{rd}^j and the basis coefficients, i.e., $\widehat{\boldsymbol{C}}_j = f_{recons}^{'}\left(t_{rd}^j\right)$. In other words, the output dimension of the model to train reduces significantly from $5N$ to M^* ($M^* \leq M \ll 5N$), which could make

the training process easier for the reconstruction.

The training data (basis coefficients), however, are only available after decomposing the temperature profiles of one layer, and such coefficients would vary significantly between layers. This indicates that the model $f'_{recons}(\cdot)$ cannot be transferred directly from one layer to another layer. Therefore, the model $f'_{recons}(\cdot)$ is constructed online for each layer, which poses a strict requirement for modeling efficiency.

In this paper, the extreme learning machine (ELM) is selected as the modeling method for $f'_{recons}(\cdot)$. ELM is a single-hidden layer feedforward neural network, which converges faster than the conventional feedforward neural network [37]. Given the training data $(\boldsymbol{X}, \boldsymbol{Y})$ and the size N_h of hidden nodes, the general formulation of ELM is presented as:

$$f_{ELM}(\boldsymbol{X}) = \Sigma_{i=1}^{N_h} \beta_i g_i(\boldsymbol{\omega}_i \boldsymbol{X} + b_i) \tag{9}$$

where β_i is the weight between the i-th hidden neuron and the output layer, and $g_i(\cdot)$ is the activation function. In ELM, only the weights $\boldsymbol{\beta} = [\beta_1, \ldots, \beta_L]$ are learned, while the parameters ($\boldsymbol{\omega}_i$ and b_i) in activation functions are assigned randomly and frozen during training. Therefore, the optimization problem to train ELM is:

$$\min_{\beta_1,\ldots,\beta_L} \|\boldsymbol{H}\boldsymbol{\beta} - \boldsymbol{Y}\|^2 \tag{10}$$

where $\boldsymbol{H}$ is a matrix containing the outputs of all hidden layers. Different from tuning both weights and activation function parameters in the iteration-based learning algorithm, ELM has much fewer parameters to learn and has no iteration, which expedites the training in general [38]. Moreover, the activation functions with random parameters could provide more statistical information about inputs and a universal approximation ability, which could provide a better generalization performance. It's proved that ELM could reach the optimal performance with a higher possibility than conventional networks [39]. Due to its outstanding performance, ELM has been applied widely in various real-time classification, clustering, and regression tasks, such as traffic flow prediction [40], transport estimation in pipes [41], and marketing price forecasting [42].

Given the relative delay and corresponding bases coefficients of all points on the layer, the input $\boldsymbol{X}$ and output $\boldsymbol{Y}$ to train the ELM model $f_{ELM}(\cdot)$ are defined as:

$$\boldsymbol{X} = \begin{bmatrix} t_{rd}^1 \\ \vdots \\ t_{rd}^M \end{bmatrix}, \boldsymbol{Y} = \begin{bmatrix} \widehat{\boldsymbol{C}}_1 \\ \vdots \\ \widehat{\boldsymbol{C}}_M \end{bmatrix} = \begin{bmatrix} c_1^1, \ldots, c_1^{M^*} \\ \vdots \\ c_M^1, \ldots, c_M^{M^*} \end{bmatrix} \tag{11}$$

After training, the basis coefficients $\widehat{\boldsymbol{C}}'$ of an unseen point p' with a relative delay t'_{rd} on the same layer could be estimated as:

$$\widehat{\boldsymbol{C}}' = f_{ELM}(t'_{rd}) \tag{12}$$

Finally, the temperature profile $\boldsymbol{P}'$ of the point p' is constructed as the product of common features $\widehat{\boldsymbol{U}}$ and the estimated coefficients $\widehat{\boldsymbol{C}}'$.

$$\boldsymbol{P}' = \widehat{\boldsymbol{U}}\widehat{\boldsymbol{C}}' \tag{13}$$

In this paper, the open-source library *elm* [43] is applied to implement the ELM model. The number of hidden nodes is set as 128, resulting in $128 \times (2 + M^*)$ parameters in the ELM model. The activation function is set as ReLu(·). And all other hyperparameters are set as the default values. For clarification, the combination of profile decomposition with POD and construction with ELM is defined as the thermal field reconstruction model $f_{recons}(\cdot)$ in further discussions.

3.4. Model fine-tuning

As discussed in Section 3.1.3, the designed numerical simulations would always differ from the actual metal AM experiments, considering the assumptions and simplifications applied in the simulations. Meanwhile, one physical metal AM printing could take hours or days, which means collecting sufficient experimental data to train data-driven models from scratch is time-consuming. To reduce the requirement of data and maintain the performance of data-driven models in physical experiments, transfer learning would be one solution. The core idea in transfer learning is to transfer the knowledge learned from sufficient source data (e.g., cheap simulation data or data from completed tasks) to the target task (e.g., new metal AM processes). Such technologies have been applied in various metal AM modeling tasks, such as melt pool size prediction [44], geometry deviation estimation [45], and defect detection [46]. More details could be found in the literature review [47].

When applying the proposed method to physical experiments, the model $f_{mapping}(\cdot)$ is pretrained based on sufficient data collected from simulations in Section 3.1.2. Several experimental data are then used to fine-tune all model parameters in the pretrained $f_{mapping}(\cdot)$ to learn the physical behavior that is not covered in the simplified simulations. In this paper, the fine-tuning process follows the same training process in Section 3.2.3. From the perspective of physical experiments, such model fine-tuning process could relax the requirement of the large experimental data size and the high accuracy of the designed simulations. The effectiveness of the proposed fine-tuning is demonstrated in Section 4.1.3.

3.5. Online prediction method for thin walls

Based on the above proposed thermal field mapping and reconstruction, this section provides an online prediction method for the thin walls with unidirectional printing to demonstrate how to solve the practical issue raised in Section 1.3. The high-level description of the online prediction method is shown in Fig. 10 and described as follows.

Stage 1: Thermal field mapping. This stage aims to train a model $f_{mapping}(\cdot)$ to learn the curve similarity between the k-th temperature curves of any point pair $\left(p_{j,i}, p_{j,i+1}\right)$. For online application, the temperature curves of points on the yet-to-print layer could be predicted from the measured temperature curves of counterpart points on the lower printed layer by $f_{mapping}(\cdot)$.
Stage 2: Thermal field reconstruction. The model $f_{recons}(\cdot)$ at this stage aims to estimate the temperature profiles of unseen points on the yet-to-print layer based on the mapped points at Stage 1, which in turn reconstructs the thermal field of the entire yet-to-print layer.

Based on the above discussions, the detailed steps of online thermal field prediction for a yet-to-print layer in the thin wall are described as follows.

Step 1: On the i-th layer, temperature profiles of M discrete points $p_{j,i}$ ($j \in [1, M]$) are measured. All profiles are then preprocessed to temperature curves $\boldsymbol{C}_{j,i}^k$ according to the description in Section 3.1.
Step 2: Under the definition of point pair in Section 2.2, the point $p_{j,i+1}$ is determined on the (i+1)-th layer. Then its partial curve $\boldsymbol{C}_{j,i+1}^{\dot{k}}$ is predicted by the pretrained thermal field mapping model $f_{mapping}(\cdot)$, as discussed in Section 3.2.
Step 3: The temperature profile of the point $p_{j,i+1}$ is constructed from the predicted curves $\boldsymbol{C}_{j,i+1}^{\dot{k}}$, as defined in Section 3.3. Then, the profile decomposition is performed to obtain the reduced basis $\widehat{\boldsymbol{U}}$ for the (i+1)-th layer and the basis coefficients $\widehat{\boldsymbol{C}}_j$ for each point $p_{j,i+1}$. Based on the data from all M points on the (i+1)-th layer, an ELM model is trained online to learn the relationship between $\widehat{\boldsymbol{C}}_j$ and the relative delay t_{rd}^j of point $p_{j,i+1}$.
Step 4: Given a new point p' on the (i+1)-th layer, its relative delay t'_{rd} could be calculated from the travel speed and the distance to the

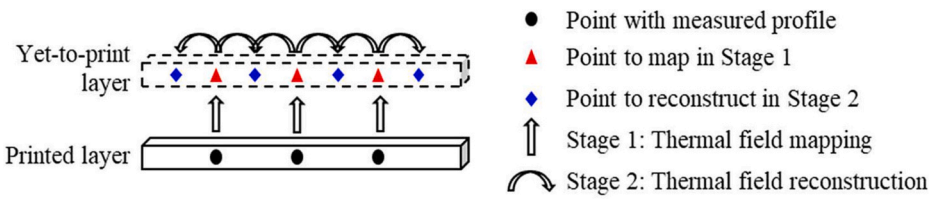

Fig. 10. High-level online thermal field prediction method.

boundary of the layer. Its basis coefficient $\widehat{C}^{'}$ is then predicted by the trained ELM model, and the temperature profile is constructed as the product $\widehat{U}\widehat{C}^{'}$.

The key feature of the proposed online thermal field prediction method is that it relies on the temperature of one printed layer, and the output of thermal field mapping is the input for thermal field reconstruction. If the thermal field of one layer could be measured during actual AM experiments, the online prediction method could be applied to predict the thermal field of any point on the yet-to-print layer. However, this method is not applicable on the first layer of AM part, as no previous layer exists. Therefore, the thermal field of the first layer is assumed to be always measured in this paper.

4. Results

Based on the collected experimental and simulation data, several steps are proposed to validate and test the proposed thermal field mapping, thermal field reconstruction, and online thermal field prediction method respectively. Given the predicted profile of one point $p_{j,i}$ based on the predicted partial curves $\widehat{\boldsymbol{P}}_{j,i} = \left[\widehat{\boldsymbol{C}}^{1'}_{j,i}, \widehat{\boldsymbol{C}}^{2'}_{j,i}, \widehat{\boldsymbol{C}}^{3'}_{j,i}, \widehat{\boldsymbol{C}}^{4'}_{j,i}, \widehat{\boldsymbol{C}}^{5'}_{j,i}\right]$, and its actual profile from FEA simulations or WAAM experiments $\boldsymbol{P}_{j,i} = \left[\boldsymbol{C}^{1'}_{j,i}, \boldsymbol{C}^{2'}_{j,i}, \boldsymbol{C}^{3'}_{j,i}, \boldsymbol{C}^{4'}_{j,i}, \boldsymbol{C}^{5'}_{j,i}\right]$, the overall performance of the predicted profile is defined below, which is denoted as the relative error of profile (REOP),

$$REOP = \frac{1}{5N}\sum_{k=1}^{5}\sum_{n=1}^{N}\frac{\left|\widehat{T}^{k',n}_{j,i} - T^{k',n}_{j,i}\right|}{T^{k',n}_{j,i}}, i \in [1,35] \tag{14}$$

where $T^{k',n}_{j,i}$ is the n-th temperature data sampled on the actual curve $\boldsymbol{C}^{k'}_{j,i}$, and $\widehat{T}^{k',n}_{j,i}$ is the n-th predicted temperature data on the predicted curve $\widehat{\boldsymbol{C}}^{k'}_{j,i}$. In theory, a smaller REOP value indicates that the predicted profile matches the actual profile with smaller deviations. In this session, N is set as 100 for all tests. Therefore, the input dimension and output dimension for the thermal field mapping model $f_{mappng}(\cdot)$ is 104 and 100 respectively, which results in 1.8635 million parameters to be learned in the model. Only the performances of points on the former 35 layers are discussed, as they can provide the required five temperature curves. To reduce the effects of randomness, all tests are performed 10 times on a desktop computer with Intel® Core™ i7-3770 CPU @ 3.40GHz processor, 24.0 GB RAM, and 64-bit Windows 10 system. All prediction results and animations among 10 runs could be found here.[1]

4.1. Validation of thermal field mapping

4.1.1. Validation with the same process setting

In this section, only Simulation 1 defined in Table 4 is studied. The data from the former 30 layers are used to train $f_{mapping}(\cdot)$, which is validated with data from the 31st to the 35th layers. Given FEA profiles of points $\left\{p_{j,i} | j \in [1,7]\right\}$ on the i-th layer ($i \in [30,34]$), the temperature profiles of points on the (i+1)-th layer are predicted by the trained thermal field mapping model, whose REOP values are summarized in Fig. 11(a). It is observed that all REOP values among 10 runs are smaller than 0.01 in most cases. The predicted profile with even the max REOP value 0.012 can capture the FEA profile successfully as shown in Fig. 11 (b). Therefore, the proposed thermal field mapping can provide accurate predictions in simulations with the same process setting.

Table 4
Details of COMSOL Multiphysics simulations.

Simulation no.	*TS* (mm/s)	*WFR* (m/min)	t_{layer} (s)	*DR* (mm³/s)	l_t (mm)
1	8	3	20.5	52.8	1.5
2	8	6	20.5	70.4	2.0
3	15	3	11.17	92.4	1.4
4	15	6	11.17	105.6	1.6
5	11	4.5	15.05	77.44	1.6
6	8	4.5	20.5	63.36	1.8
7	15	4.5	11.17	99	1.5
8	11	3	15.05	72.6	1.5
9	11	6	15.05	87.12	1.8

4.1.2. Validation with different process settings

To explore the applicability of the proposed thermal field mapping among different process settings, all processed profiles from Simulation 1–4 and Simulation 6–9 are used to train the model. For the i-th layer ($i \in [2,34]$) in Simulation 5, the temperature profiles are estimated by the trained mapping model based on the FEA profiles on the (i-1)-th layer.

The boxplots of REOP values in all runs are shown in Fig. 12(a). The overall REOP values reduce with the layer number, which reflects better accuracy on higher layers. This behavior is attributed to the increased curve similarity as discussed in Section 3.2. For any layer above the 10th layer, the median REOP value is smaller than 0.01. Comparing the predicted temperature profile with the max REOP value 0.0548 and its corresponding FEA profile in Fig. 12(b), the prediction provided by the pretrained model can capture the thermal trend accurately, although some deviations would occur at the temperature peaks. Therefore, we can claim that the thermal field mapping has the generalization capability to predict the thermal field of yet-to-print layers among different process settings.

4.1.3. Test on experimental data

The model $f_{mapping}(\cdot)$ in Section 3.2 is designed to learn the curve similarity between two successive layers, while the temperature profiles are measured at one point every five layers in the designed CMT-WAAM experiments as mentioned in Section 3.1.1. This indicates that it is not reasonable to apply the trained model $f_{mapping}(\cdot)$ to the experimental curves directly. Therefore, a recursive prediction method is designed to predict the experimental temperature curves of the point on the (i+5)-th layer from the counterpart on the i-th layer, as shown in Fig. 13. For instance, given one temperature curve $\boldsymbol{C}^{k}_{1,1}$ of the middle point on the first layer, the partial temperature curve of the middle point on the

[1] https://drive.google.com/file/d/1PN1ex1uaBMuLg8zWrE4LJMFt4KJ5XUZ4/view?usp=sharing.

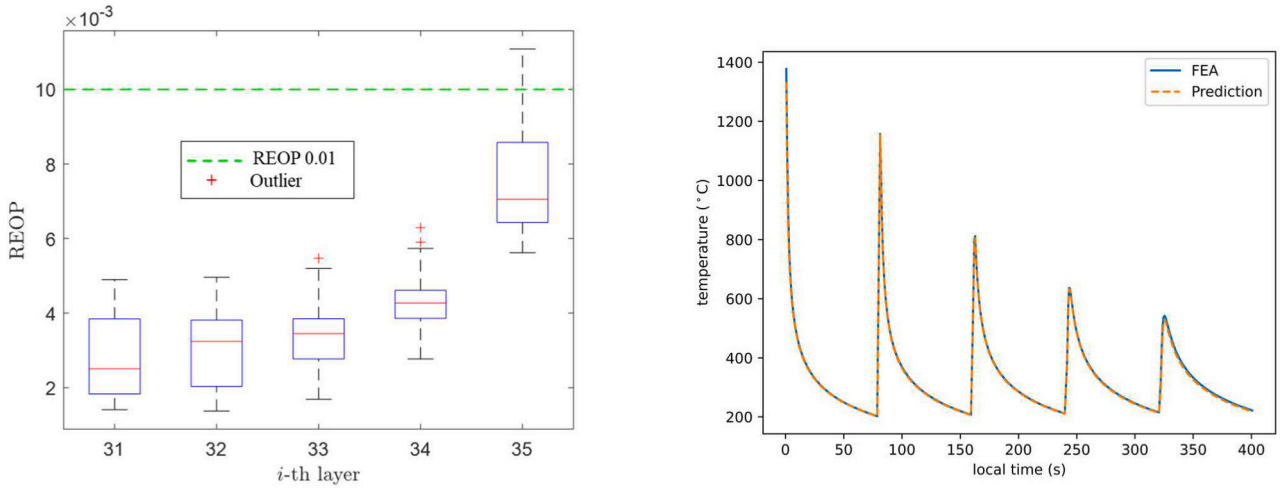

(a) Boxplots of REOP values (b) Profile with the max REOP 0.012

Fig. 11. Validation results of thermal field mapping on Simulation 1.

Table 5
Training process of FCN-RC.

Input: training data $(\boldsymbol{X},\boldsymbol{Y})$ where $\boldsymbol{X}$ is the input matrix with size $N_s \times (N+4)$, $\boldsymbol{Y}$ is the output matrix with size $N_s \times N$, the total epoch number $epoch_{total} = 500$, batch size $b = 256$, learning rate $lr = 0.001$, shrinking ratio $r = 0.5$, initialized model $f_{mapping}(\cdot)$

Output: the trained model $f_{mapping}(\cdot)$

For $epoch$ in [1, $epoch_{total}$]
  Divide the training data into batches according to the batch size, i.e., $\boldsymbol{X}_B, \boldsymbol{Y}_B = sampling(\boldsymbol{X},\boldsymbol{Y},b)$,
  For all $\boldsymbol{X}_B^i, \boldsymbol{Y}_B^i$ in $\boldsymbol{X}_B, \boldsymbol{Y}_B$, where $\boldsymbol{X}_B^i$ has the size $b \times (N+4)$ and $\boldsymbol{Y}_B^i$ has the size $b \times N$
    Get the predicted value $\widehat{\boldsymbol{Y}}_B^i = f_{mapping}(\boldsymbol{X}_B^i;\theta)$, where θ refers to the parameters to learn
    Get the mean square error loss $e = MSE(\widehat{\boldsymbol{Y}}_B^i, \boldsymbol{Y}_B^i)$
    Update the model parameters based on Adam optimizer, i.e., $\theta = Adam(\theta, e, lr)$
  End
  If $epoch \in \{100,200,300,400\}$
    $lr = lr \times r$
  End
End

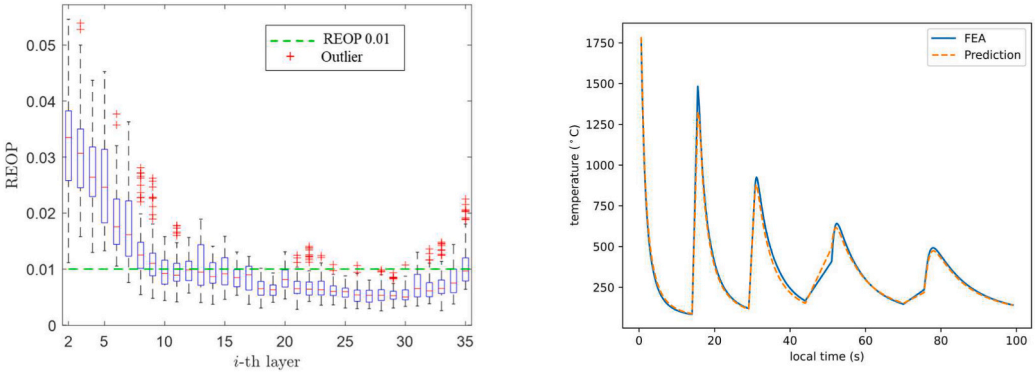

(a) Boxplots of REOP values (b) Profile with the max REOP 0.0548

Fig. 12. Validation results of thermal field mapping on Simulation 5.

second layer is predicted as $\widehat{\boldsymbol{C}}_{1,2}^{k'} = f_{mapping}\left(\boldsymbol{C}_{1,1}^{k}, t_{layer}, t_{dwell}^{1}, DR, h_1\right)$, based on which the corresponding partial temperature curve of the middle point on the third layer could be estimated as $\widehat{\boldsymbol{C}}_{1,3}^{k'} = f_{mapping}\left(\widehat{\boldsymbol{C}}_{1,2}^{k'}, t_{layer}, t_{dwell}^{2}, DR, h_2\right)$. This prediction process continues until obtaining the partial curve of the middle point on the sixth layer, i.e., $\widehat{\boldsymbol{C}}_{1,6}^{k'} = f_{mapping}\left(\widehat{\boldsymbol{C}}_{1,5}^{k'}, t_{layer}, t_{dwell}^{5}, DR, h_5\right)$. Then the REOP value of the predicted partial curve $\widehat{\boldsymbol{C}}_{1,6}^{k'}$ is calculated based on the experimental partial curve $\boldsymbol{C}_{1,6}^{k'}$ with the same time duration.

Theoretically, large prediction errors are anticipated if the designed recursive prediction method is tested on the experimental curves

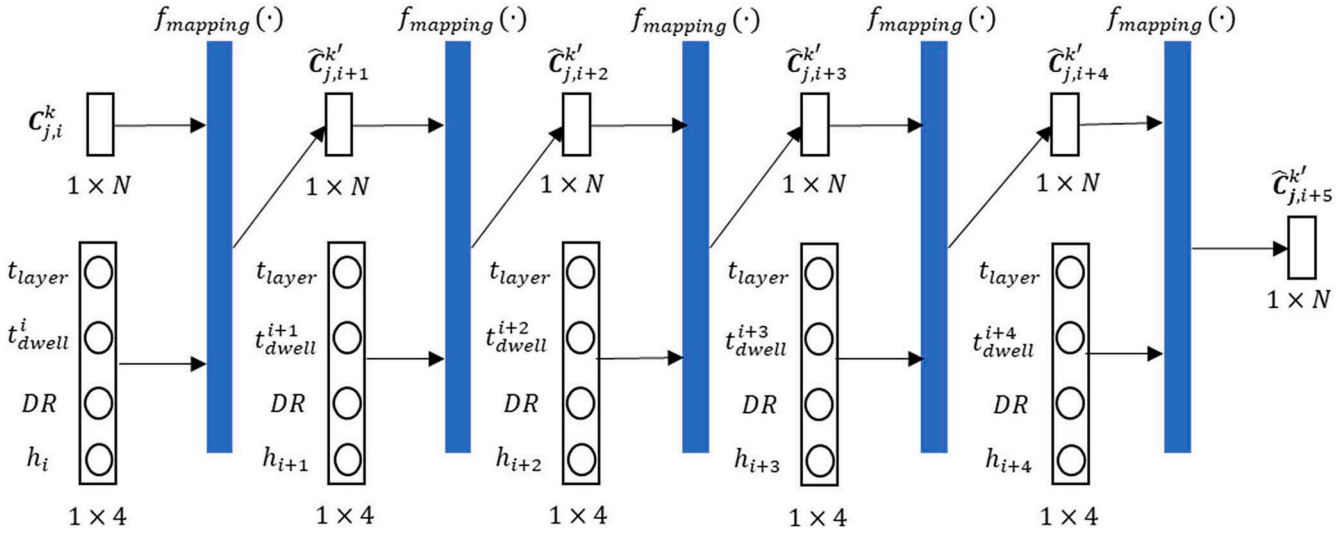

Fig. 13. Recursive prediction method for experimental temperature curves.

directly, considering the following two factors.

(a) *Simplified thermal behavior in simulations.* Generally, the thermal behavior in WAAM experiments is more sophisticated than the one in FEA simulations. Many assumptions have been applied in the FEA simulation for simplification, such as no geometry deformation, constant energy input, and fixed process parameters during printing. However, the geometry deformation and dynamic process parameters (e.g., travel speed, wire feed rate) during printing would make the experimental thermal behavior quite different from the one in simulations.

(b) *Error accumulation during recursive prediction.* In the proposed recursive prediction method, the prediction error on the partial

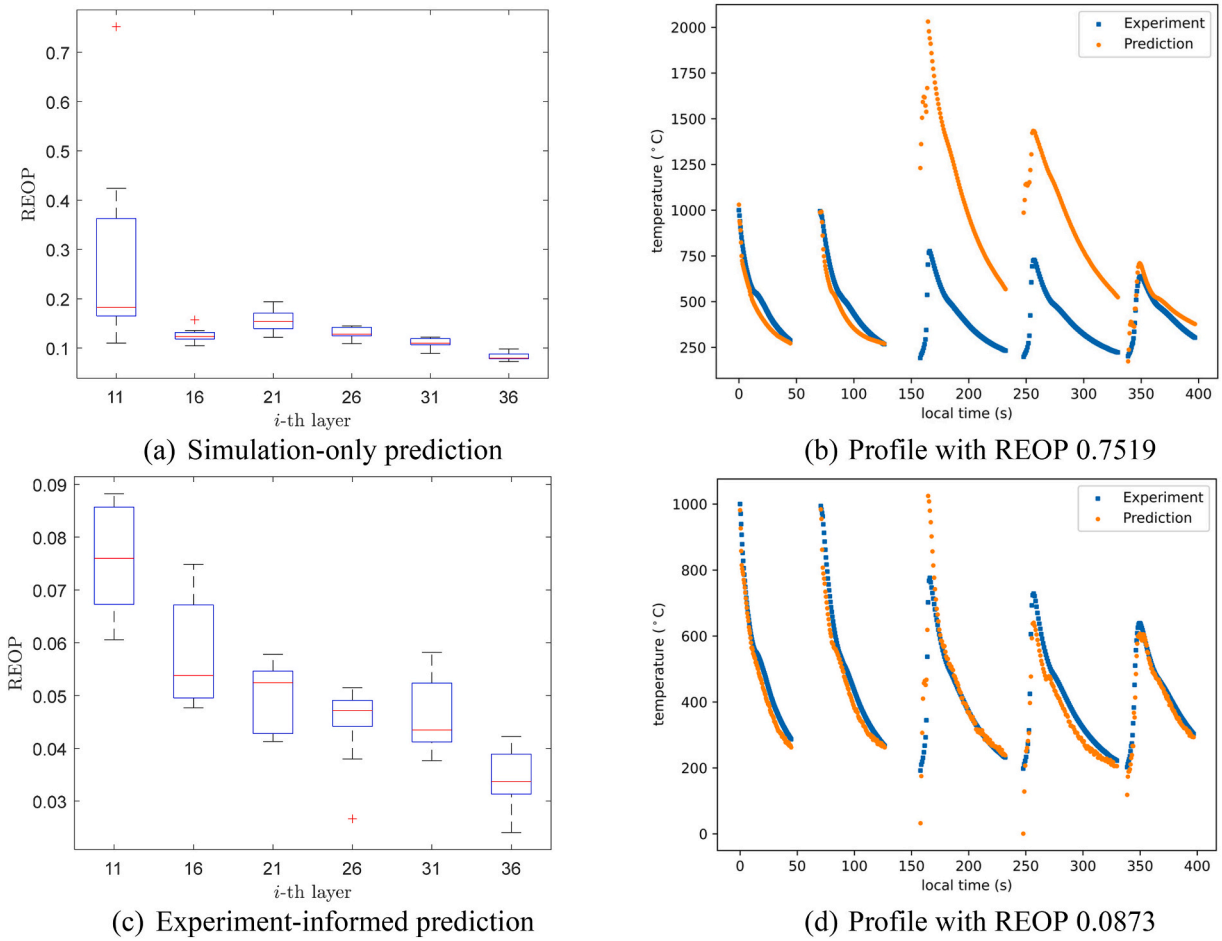

Fig. 14. Prediction performance of $f_{mapping}(\cdot)$ on the 8th experiment.

curve $\widehat{C}^{k'}_{j,i+1}$ would be passed to the next prediction $\widehat{C}^{k'}_{j,i+2}$. Therefore, the error caused by the simplified thermal behavior would be amplified in the final prediction $\widehat{C}^{k'}_{j,i+6}$.

To study the effect of the above two factors on the prediction performance, two test cases are defined for comparison.

(a) *Simulation-only prediction*: After training the thermal field mapping model $f_{mapping}(\cdot)$ with 11,340 temperature curves from all nine simulations, the trained model $f_{mapping}(\cdot)$ is tested with temperature curves obtained from Experiment 8. Therefore, no physical information about the actual experiment is contained in the trained model $f_{mapping}(\cdot)$.
(b) *Experiment-informed prediction*: After training $f_{mapping}(\cdot)$ with all simulation data, the model fine-tuning process in Section 3.4 is applied to update the $f_{mapping}(\cdot)$ based on the 115 temperature curve pairs from Experiment 1–7 and Experiment 9–15. As a result, the fine-tuned model learns some information about the physical thermal behavior in actual CMT-WAAM experiments.

The performance of both simulation-only and experiment-informed predictions is summarized in Fig. 14. In general, the performance of the experiment-informed prediction outperforms the simulation-only prediction significantly. The REOP values of predicted profiles in the simulation-only prediction are larger than 0.1 in most cases, and the outlier REOP value could reach 0.75, as shown in Fig. 14(a). The predicted profile with the outlier REOP value is shown in Fig. 14(b), where the first and the second curves match the experimental curves well. But the third and the fourth curves have a large deviation, and the predicted temperature value is twice the experimental value. The observed worse performance can be explained from three factors. First, the trained model $f_{mapping}(\cdot)$ in the simulation-only prediction cannot capture certain behavior in physical experiments, considering some assumptions (i.e., fixed layer thickness, no geometry deviation) applied in the simulation. Second, the third curve of the point on the sixth layer has a short plateau of temperature 1000 °C as shown in Fig. 15(a), which is quite different from the third curve of the point on the 11th layer as shown in Fig. 15(b). As the thermal field mapping is designed for similar curves, the performance would deteriorate when applied to dissimilar curves. The last reason is that the pyrometer is moving manually during experiments, which contributes to the dissimilar temperature curves in Fig. 15 and brings some unmeasurable uncertainties (e.g., point location on the layer) to the thermal field mapping. Those uncertainties are not covered in the designed input variables. As a result, the profile obtained by the simulation-only prediction is unacceptable and cannot be applied in online applications directly.

In contrast, the REOP values of all predicted profiles from the experiment-informed prediction are smaller than 0.09, as shown in Fig. 14(c). Same to the phenomenon in the FEA simulations, the prediction performance also increases with the layer number in experiments, which indicates that the experimental curve similarity increases with the height. Besides, the profile with the max REOP 0.7519 in the simulation-only prediction has a REOP value 0.0873 in the experiment-informed prediction, as shown in Fig. 14(d). Compared with Fig. 14(b), all predicted temperature curves match the experimental ones better. This demonstrates that the proposed thermal field mapping model could be applied in actual CMT-WAAM experiments after learning actual physical thermal behavior. Besides, compared with the training data size from simulations (i.e., 11,340), the size of experimental data (i.e., 115) for fine-tuning is quite small, which reflects the generalization capability of the proposed thermal field mapping model in both simulation and experiments.

4.2. Verification of thermal field reconstruction

To verify the proposed method in Section 3.3, the FEA profiles from points $p_{1,i}$, $p_{3,i}$, $p_{5,i}$, and $p_{7,i}$ on the i-th layer ($i \in [1, 35]$) are selected to train a thermal field reconstruction model. Then the profiles of points $p_{2,i}$, $p_{4,i}$, and $p_{6,i}$ are predicted and compared with the corresponding FEA profiles.

The REOP values of predicted profiles on each layer among 10 runs are summarized in Fig. 16, where two phenomena could be observed. First, most of the REOP values are smaller than 0.02, although some outliers are observed on each layer. As shown in Fig. 17, the smaller the REOP value, the smaller differences are between the profiles. When the REOP value is around 0.1, the difference between the FEA profile and the prediction is observable visually, as shown in Fig. 17(a). When the value is around 0.03, the difference in profiles is visually undetectable, as shown in Fig. 17(b). Second, the overall prediction performance improves with the layer number. Below the fifth layer, the median REOP value of one layer is always larger than 0.01 (the green dashed line in Fig. 16); above the fifth layer, the median REOP value is smaller than 0.01. Meanwhile, the size of the box also reduces with the increase of the layer number. According to Section 3.3, the performance of the proposed thermal field reconstruction model (i.e., POD based ROM with ELM) is affected by the linearity of the profiles on the same layer. If the linearity is higher, the prediction performance would be better. In other words, the second phenomenon indicates that the linearity among temperature profiles also increases with the increasing layer number. One possible reason is that the thermal behavior is more stable on higher layers considering the heat accumulation on the lower layers. The above

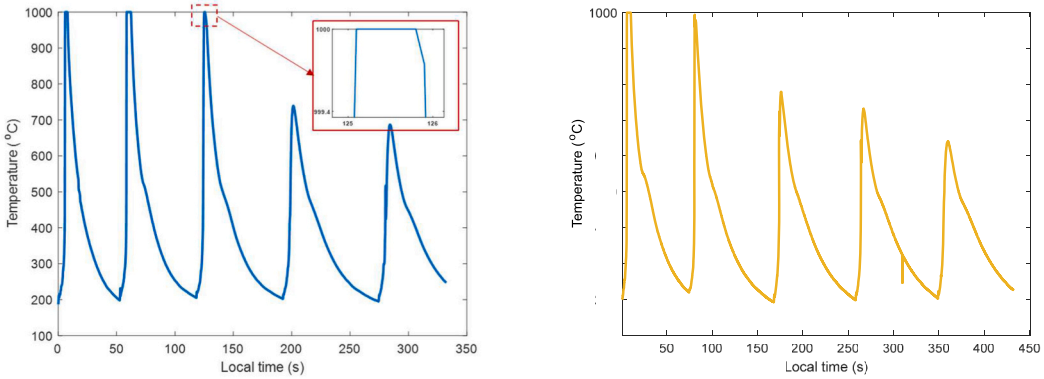

(a) Raw experimental profile of the 6th layer (b) Raw experimental profile of the 11th layer

Fig. 15. Temperature profiles of the 6th layer and the 11th layer in Experiment 8.

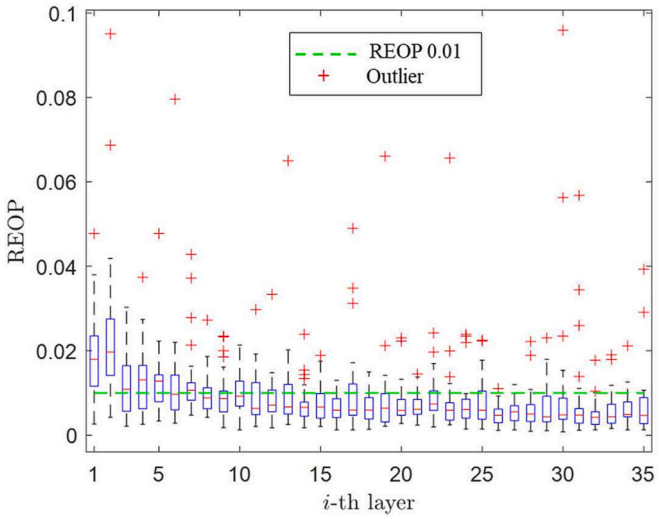

Fig. 16. Boxplots of REOP values from points on different layers.

discussions demonstrate that the thermal field reconstruction model enables the construction of the temperature profiles with acceptable accuracies.

4.3. Validation of online thermal field prediction

As the generalization capability of mapping and reconstruction strategies is discussed in Sections 4.1 and 4.2, respectively, this section aims to demonstrate the generalization capability of the online thermal field prediction method that encompasses these two strategies for metal AM with the same or different process settings.

4.3.1. Validation with the same process setting

In this subsection, temperature profiles of the former 30 layers (i.e., 1015 curve pairs) from Simulation 1 are used to train the thermal field mapping model $f_{mapping}(\cdot)$ first. Given the i-th layer ($i \in [31, 35]$), temperature curves of points $p_{1,i}$, $p_{3,i}$, $p_{5,i}$, and $p_{7,i}$ are predicted by the trained model $f_{mapping}(\cdot)$ from FEA curves of points on the (i-1)-th layer. Then the thermal field reconstruction model $f_{recons}(\cdot)$ is applied to construct the temperature profiles of points $p_{2,i}$, $p_{4,i}$, and $p_{6,i}$, whose REOP values reflect the overall performances of the online thermal field prediction method on the i-th layer.

The boxplots of REOP values on each layer among 10 runs are shown in Fig. 18. The median REOP values of all layers are smaller than 0.01, which indicates that the constructed temperature profile could match well the temperature profile from FEA in most cases, as shown in Fig. 19 (b). Although the outlier REOP value 0.1294 refers to an unacceptable profile with obvious deviations to the profile from the FEA simulation, the overall trend on the temperature profile is captured successfully, as shown in Fig. 19(a).

Besides, to reflect the performance of the proposed method on constructing the thermal field of the entire layer, the thermal field reconstruction model is used to construct the profiles of 160 points evenly located on the 31st layer, based on the FEA profiles and the predicted profiles of all seven points on the same layer. Then the temperature field is constructed according to the relative delays of all 160 points, and the temperatures of points which are not printed are assumed to be the room temperature. As only points located on the side of the layer are measured, the temperature inside the layer is not recorded in this work. For simplification, all points within the layer are assumed to behave the same along the width direction, i.e., holding the same temperature. Fig. 20 depicts the temperature field of the 31st layer at different local times, where the time starting to print the layer is defined as the local time 0. From the temperature field at local time 6.0 s, some differences are observed near the boundary (i.e., the starting and ending point) of the layer. The reason is that the boundary points of the layer are not covered to record temperature profiles, as shown in Fig. 4. Then the prediction error could be amplified when extrapolating the temperature field near the boundary from the predicted profiles of points $p_{j,i}$ ($j \in [1, 7]$). At local times 93.0 s, the temperature fields of the layer constructed from both FEA and predicted profiles seem identical, especially in the region away from the boundary.

To sum up, the proposed online thermal field prediction method could predict the thermal field of the entire higher layer from the profiles of several points located on the lower layer, when the simulation settings (e.g., wire feed rate, travel speed, interpass temperature) of both training and testing data are the same. In other words, if the model could be trained based on profiles from the printed layers, the thermal field of the yet-to-print could be predicted with acceptable accuracies, i.e., most REOP values of predicted profiles are smaller than 0.01.

4.3.2. Validation with different process settings

In this section, the training and testing data are collected from different simulations, to study the generalization capability of the online thermal field prediction method among different process settings. More specifically, the thermal field mapping model $f_{mapping}(\cdot)$ is trained on the 10,080 curve pairs from Simulations 1–4 and Simulations 6–9. For Simulation 5, temperature profiles of points $p_{2,i}$, $p_{4,i}$, and $p_{6,i}$ on the i-th

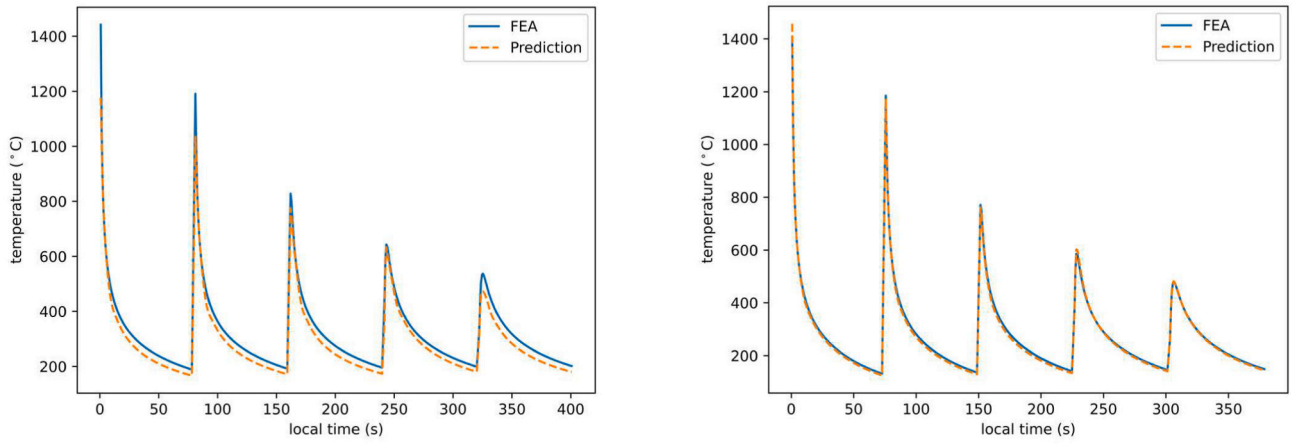

Fig. 17. Comparison of FEA profiles and predicted profiles in testing $f_{recons}(\cdot)$ only.

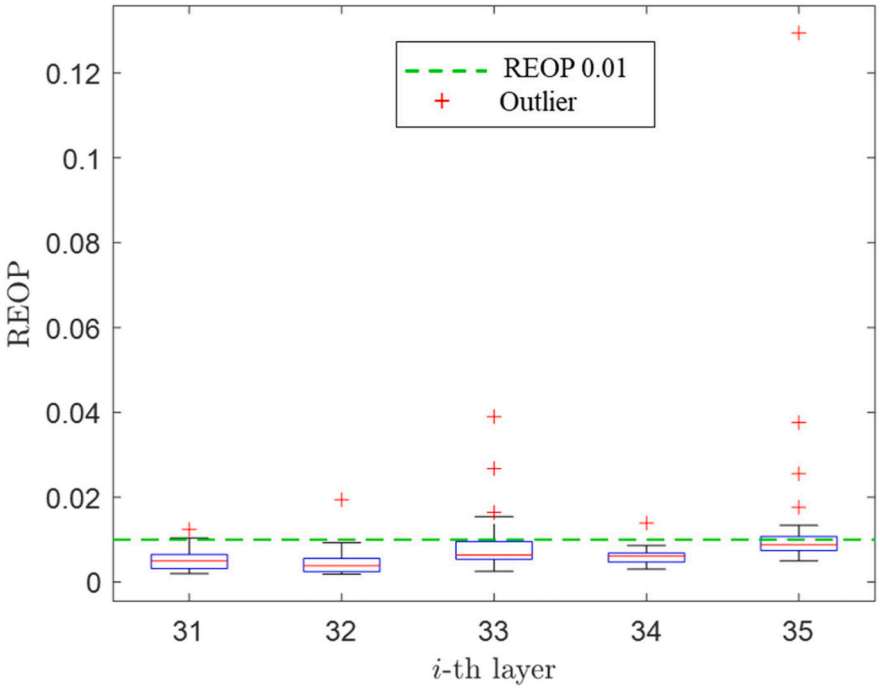

Fig. 18. REOP of profiles on higher layers in validation with the same process setting.

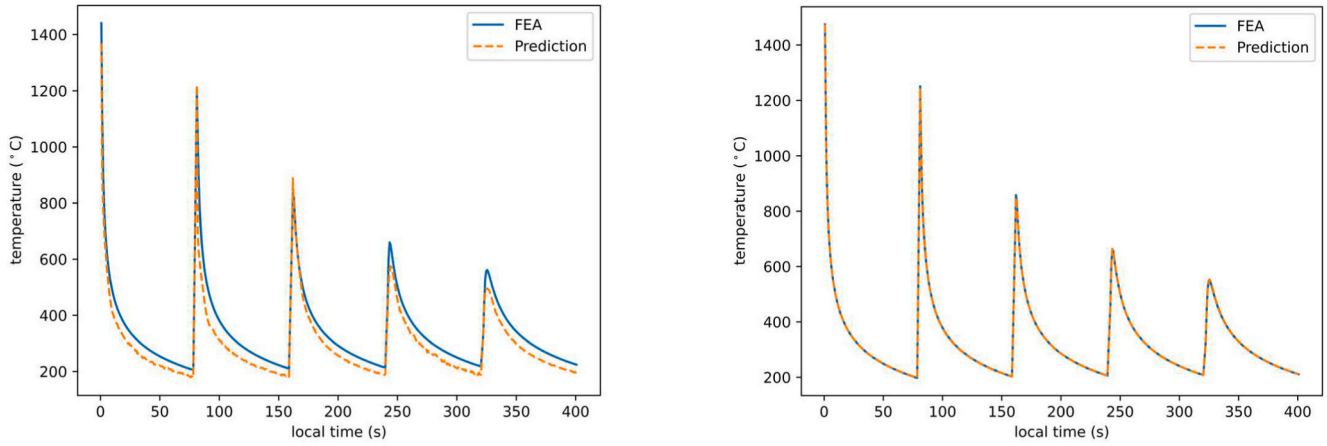

Fig. 19. Comparison of FEA and predicted profiles in validation with the same process setting.

layer ($i \in [2, 35]$) are constructed by the thermal field reconstruction model from points $p_{1,i}$, $p_{3,i}$, $p_{5,i}$, and $p_{7,i}$, whose temperature profiles are predicted directly by the trained model $f_{mapping}(\cdot)$ from the FEA profiles on the (i-1)-th layer. The REOP values at points $p_{2,i}$, $p_{4,i}$, and $p_{6,i}$ are selected to indicate the overall performance of the proposed method on the layer.

Fig. 21 shows the boxplots of obtained REOP values from the second to the thirty-fifth layer. Similar to the results in Fig. 16, the overall performance of one layer increases with the height, which is attributed to the increased curve similarity between two successive layers (Section 3.2) and the increased linearity among temperature profiles on the same layer (Section 4.2). When testing the proposed method on the unseen simulation setting, the overall performance decreases compared with the performances in Sections 4.2 and 4.3.1. For example, the max outlier REOP value 0.1398 in the validation with different process setting is 46 % larger than the max value 0.0959 in Fig. 16. From the comparison in Fig. 22(a), the predicted profile has a large deviation on the peaks at the profiles. The maximum value at the first predicted curve is around 2200 °C while the value from the FEA model is below 1500 °C indicating an error over 700 °C. Besides, the box sizes from the 31st layer to the 34th layer in the validation with different process settings (Fig. 21) are larger than the box sizes obtained in the validation with the same process setting (Fig. 18). Although the median REOP values on the former five layers are larger than 0.02 in the validation with different process settings, all median REOP values are smaller than 0.01 above the 18th layer, and most REOP values are smaller than 0.02 above the eighth layer. The predicted profile with the median REOP value 0.0103 is shown in Fig. 22(b), where the predicted profile still matches well with the profiles from the FEA simulation.

Similar to Section 4.3.1, the FEA profiles and predicted profiles of points $p_{j,i}$ ($j \in [1, 7]$) are used to construct the thermal field of the 10th and the 20th layer. In this section, only temperature fields of the 10th and the 20th layer at two different local times are shown in Figs. 23 and 24 respectively. Same as the observation in Section 4.3.1, the difference

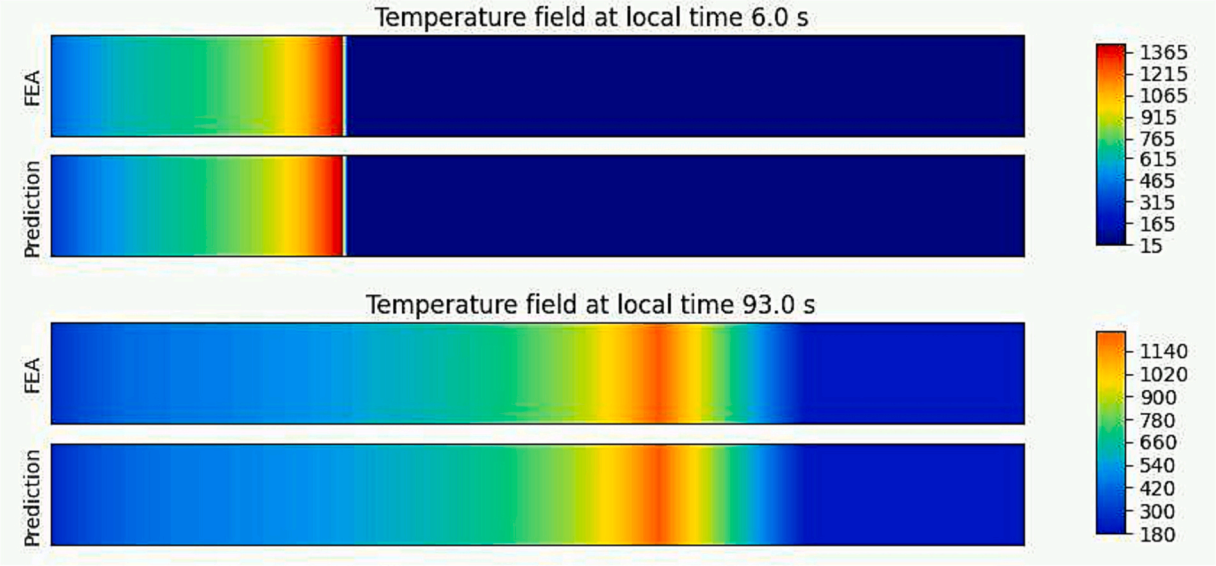

Fig. 20. Temperature field of the 31st layer in validation with the same process setting.

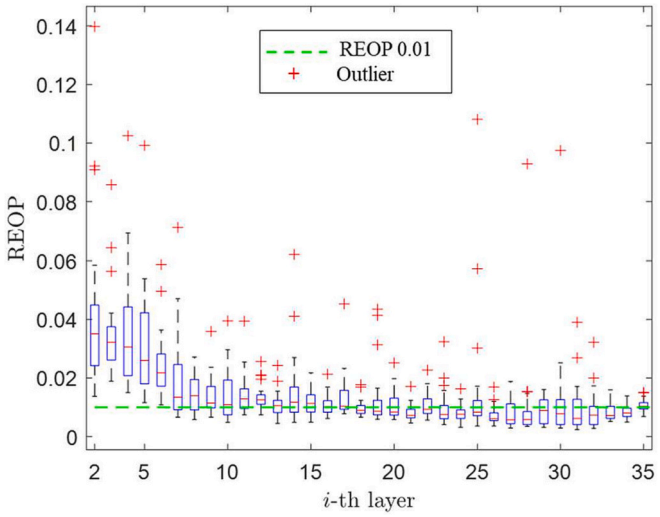

Fig. 21. REOP of profiles on layers in validation with different process settings.

near the boundary points also exists on both layers. Although some deviations are found in the temperature field, the trend of the entire layer is captured successfully on both layers, which indicates its capability to predict the thermal field of the higher layers in simulations with new process settings.

Therefore, after training with sufficient data from simulations, the proposed online thermal field prediction method could be used to predict the thermal field of the higher layer when simulating the WAAM process with new parameters. This scenario is similar to online applications. If sufficient temperature profiles are collected from WAAM experiments to train the thermal field mapping model, the online prediction method in Section 3.5 could be used in other WAAM experiments with new process settings to predict the thermal field of the entire yet-to-print layer online, which is useful for in-situ monitoring and control.

4.4. Computational efficiency

Above discussions have demonstrated the generalization capability of the proposed methods. As they are designed for online applications, the required CPU time for execution is another important factor. Given a trained thermal field mapping model $f_{mapping}(\cdot)$, the CPU time required

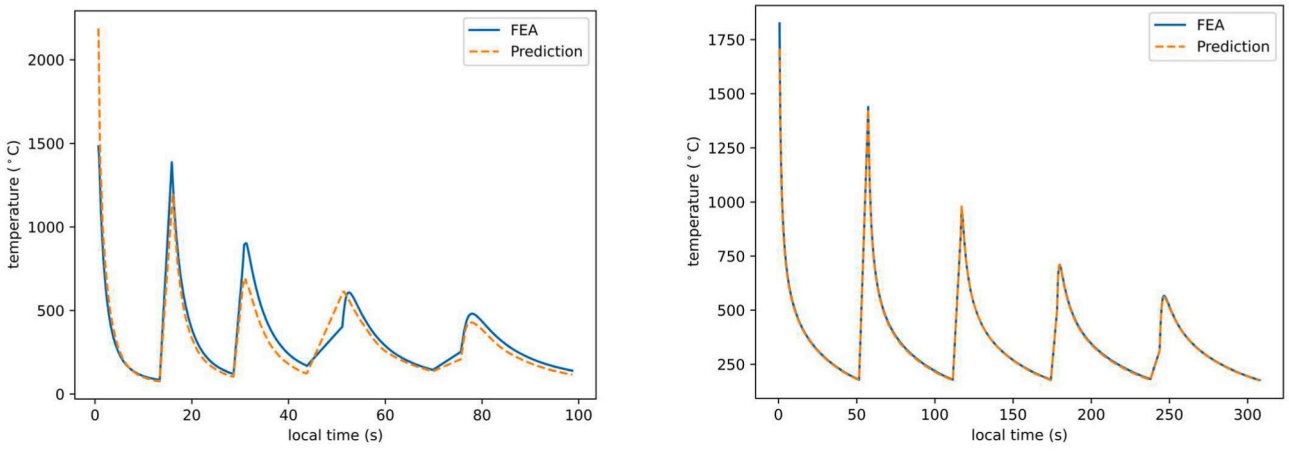

(a) Max REOP 0.1398 (b) Median REOP 0.0103

Fig. 22. Comparison of FEA and predicted profiles in validation with different process settings.

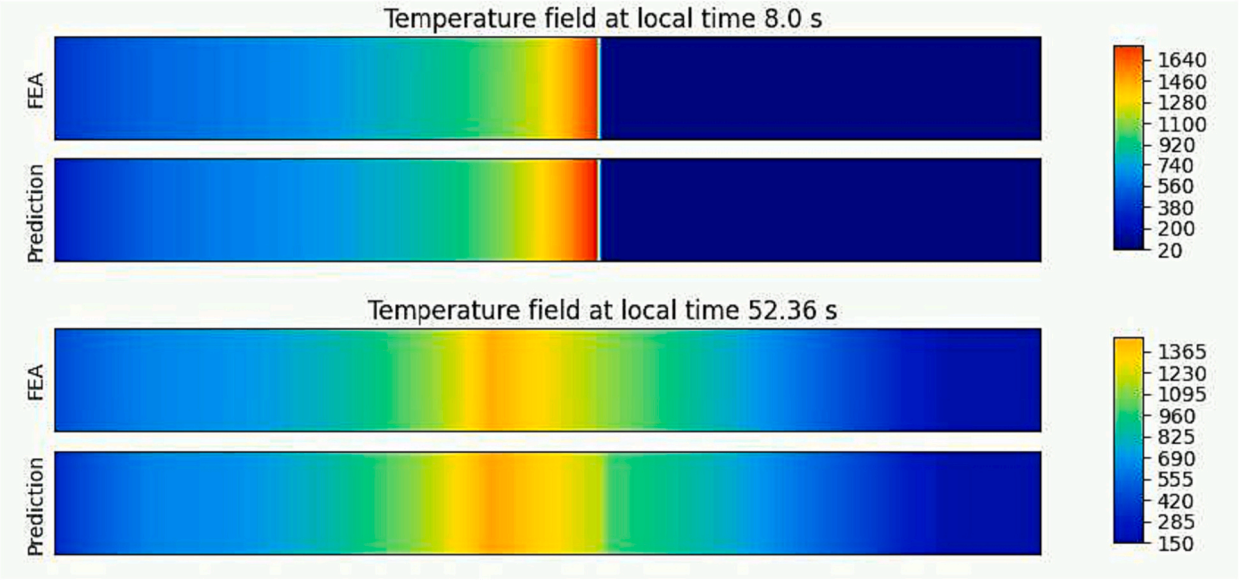

Fig. 23. Temperature field of the 10th layer in validation with different process settings.

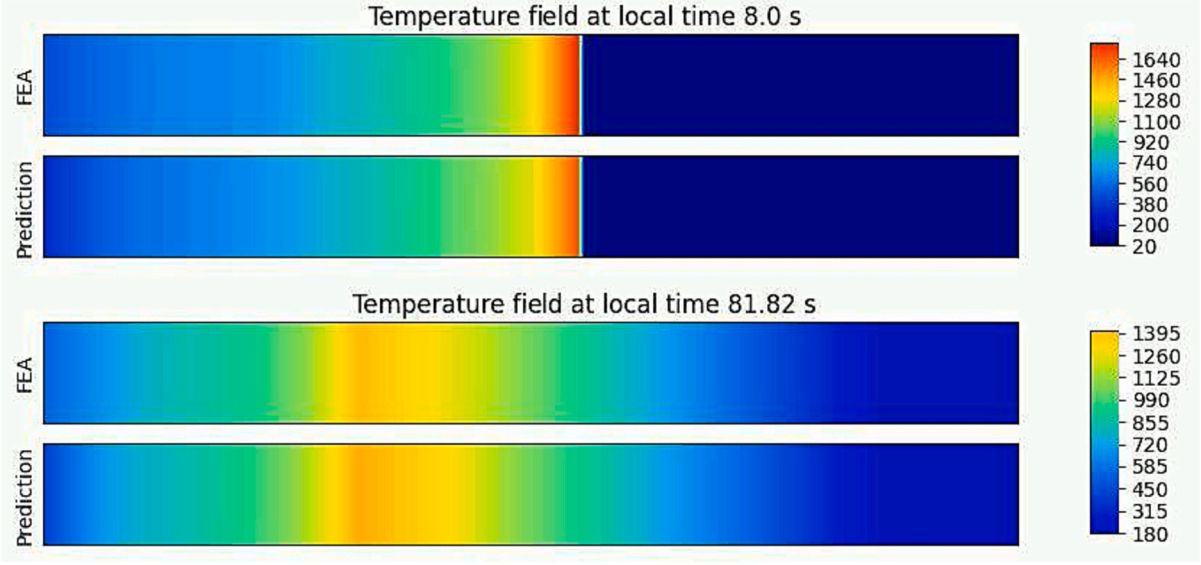

Fig. 24. Temperature field of the 20th layer in validation with different process settings.

for prediction increases with the number of testing curves, as shown in Fig. 25(a). In this paper, seven points are located on one layer and each point has five temperature curves. Only <0.01 s is required to predict total 35 temperature curves from the curves on the lower layers. The execution time to construct the profiles of three points by the thermal field reconstruction model $f_{recons}(\cdot)$ on each layer is summarized in Fig. 25(b), where the time on each layer is smaller than 0.02 s in most cases. Therefore, the total execution time of the proposed online thermal field prediction method would be smaller than 0.1 s. Considering the dwell time of each layer varies from seconds to minutes during the completed CMT-WAAM experiments, the proposed prediction method is promising to be applied to the in-situ control or monitoring tasks.

4.5. Summary remarks

Based on the above testing and discussion, three conclusions could be drawn about the proposed online thermal field prediction method: (a) The proposed method is efficient, as the execution CPU time to construct the thermal field of one layer from the temperature profile on the lower layer is <0.1 s on a commodity desktop computer (Intel Core i7-3770 CPU @ 3.40GHz processor, 24.0 GB RAM); (b) The proposed method has acceptable performances in simulation data, whether or not the training and testing data are from the simulation with the same process parameters; and (c) The proposed thermal field mapping model can provide acceptable prediction performance on actual WAAM experiments after learning the physical thermal behavior from some experimental data. Therefore, we can claim that the proposed online thermal field prediction method is promising for online applications as far as the thermal field is concerned.

5. Discussions

Although the online thermal field prediction method shows great performance in the thin wall printed unidirectionally, both thermal field mapping and reconstruction have some limitations, which are discussed in the following sections, along with their possible applications beyond a

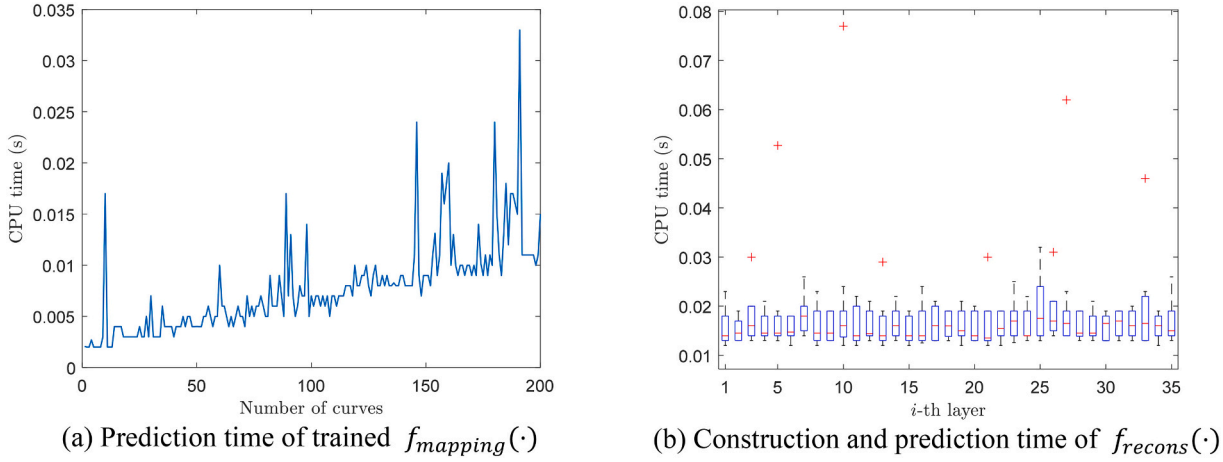

Fig. 25. CPU time to execute the online prediction method.

thin wall.

5.1. Thermal field mapping

In this paper, the thermal field mapping in Section 3.2 is only designed based on the observed curve similarity. According to the results in Section 4.1, the proposed method could capture the temperature profiles on the yet-to-print layer in both simulations and experiments, when the similar thermal behavior is observed. However, the prediction of the thermal field mapping would deviate from reality when dissimilar temperature curves are studied, such as the third curve in Figs. 14 and 15. Therefore, the proposed thermal field mapping cannot be applied to cases with dissimilar temperature curves, such as the successive layers with various geometries (e.g., corner, intersections, hollow ellipse) in complex parts and successive layers with different toolpaths.

Although the thermal field mapping is limited to applications with similar temperature curves and only tested in the unidirectionally printed thin wall, several potential applications could be anticipated, followed with some possible solutions.

(a) *Single layer with a periodic toolpath*. When printing one layer without holes, periodic toolpaths (e.g., zigzag, contour parallel) could be applied as shown in Fig. 26, which would bring periodic physical behavior to points on the toolpath. For those cases, the point pair mentioned in Section 2 could be defined based on the periodicity in the toolpath. Shown as the dots in Fig. 26(a), the point pair is defined according to points with the same relative position on two zigzags. When the successive periodic toolpaths have different lengths, each toolpath could be scaled to the same length (e.g., the max one) and the points with the same relative location on the scaled toolpath could be defined as the point pair, as shown in Fig. 26(b) and (c). In such cases, other input variables (e.g., scaled ratio and deposition time) should be defined according to the toolpath to reflect their effects on the temperature curve similarity.

(b) *Three-dimensional (3D) geometry with a constant/periodic toolpath*. For products with simple geometries (e.g., cube, cylinder), a constant toolpath could be applied on each layer, or the toolpath would repeat every several layers. As a result, the thermal behavior on successive layers or on several discrete layers would also be periodic to some extent. For more complex 3D geometries, certain geometries may be divided into segments of simple geometries along the vertical direction and within each segment toolpaths would have certain periodicity. In the above cases, the proposed thermal field mapping could be then applied to predict the temperature profiles online according to the anticipated similarity. As those geometries are more complex than the thin wall studied in the paper, more features should be considered as the input variables to cover the effects of geometries on the thermal field mapping.

Based on above discussions, the generalization of the proposed thermal field mapping would be tested on other geometries and toolpaths based on more simulations and experiments in the future study. Moreover, its performance in other metal AM processes (e.g., DED) should be explored. Apart from the thermal field, the capability of the mapping method should be studied on other online measurable properties that also show periodicity and similarity, such as the melt pool

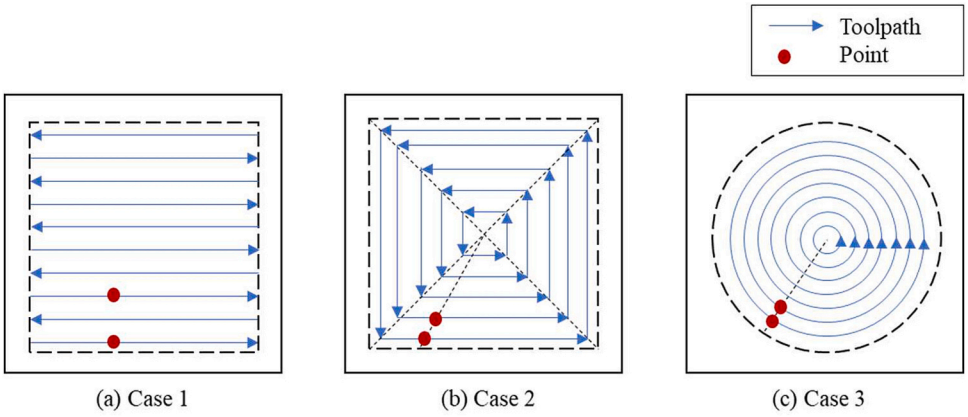

Fig. 26. Single layer with a periodic toolpath.

size.

5.2. Thermal field reconstruction

Different from the thermal field mapping, the proposed thermal field reconstruction does not depend on the profile similarity of points on the same layer. The thermal field reconstruction method, i.e., reduced order model with extreme learning machine, is a high-dimensional response decomposition and reconstruction method in essence. Similar methods have been studied widely in other fields [33–35].

When applying the proposed method to reconstruct the thermal field of the entire part (e.g., one layer with an arbitrary geometry) based on a few measured points, its prediction performance and capability would be limited by two factors, i.e., the number of measured points, and the linearity between temperature profiles of different points. When the number of measure points is small, the captured reduced bases (i.e., temperature profile features) are too few to represent the thermal behavior of all points in the entire part. As a result, the reconstructed thermal field of the entire part would deviate far from the actual value. In addition, according to the description in Section 3.3, the reconstructed temperature profile could be considered as a linear combination of measured temperature profiles. However, such linearity cannot be guaranteed when a complex geometry and a different toolpath are applied. To tackle this limitation, the autoencoder based UNet model was applied to reduce the dimension of fluid dynamic responses and the reduced order modeling was performed on the low-dimensional encoded latent features instead of the raw data [48]. Similar ideas could be combined with the thermal field reconstruction to improve its capability for different geometries and toolpaths.

To sum up, the proposed thermal field reconstruction method could be applied to the part with any geometry and toolpath. To improve the prediction performance, some methods (e.g., deep learning models) could be adopted to store the nonlinearity relationship between the temperature responses of measured points, after which the reduced order model is constructed based on the low-dimensional preprocessed data. Similar to the thermal field mapping, the capability of the thermal field reconstruction would be tested with various geometries, toolpaths, and metal AM processes in future studies.

6. Conclusions

Different from current data-driven thermal field modeling methods based only on simulations, this paper addresses the research issue — *how to predict the thermal field of yet-to-print parts online when only a few sensors are available for meal AM*. This paper proposes an online thermal field prediction method based on mapping and reconstruction. This method is tested with both simulation and actual metal printing data. First, similarities between temperature curves of two successive layers (i.e., curve similarity) and temperature profiles of points on the same layer (i.e., profile similarity) are analyzed. Then, nine simulations in COMSOL Multiphysics software and fifteen wire arc additive manufacturing experiments are completed with corresponding profile processing methods, followed by comparisons between simulations and experiments. Based on the observed curve similarity, the thermal field mapping builds a fully connected artificial neural network with residual connection to predict the temperature curves of points on the yet-to-print layer from the measured temperature curves of the previously printed layer. Given measured/predicted temperature profiles of several points on the same layer, the thermal field reconstruction applies the reduced order model (ROM) to predict the temperature of every point on the layer. The computationally efficient extreme learning machine is selected to train the ROM. Then a model fine-tuning process is proposed to update the model pretrained on simulations with limited experiment data to improve the model performances for physical printings.

Based on the test results, three observations are made:

(a) The proposed online thermal field prediction method is computationally efficient since the time to construct the thermal field of one layer is within 0.1 s on a low-cost desktop computer.
(b) The proposed work has good generalization performance within the same simulation of the same AM process parameters and among simulations with different process parameters.
(c) After fine-tuning with limited experimental data, the trained method predicts the thermal field of yet-to-print layers of physical experiments with small relative errors.

All test results demonstrate that the proposed online thermal field prediction method is promising for online thermal prediction and ultimately the control of metal AM processes.

Finally, the limitations and possible applications of the two core components, i.e., thermal field mapping and reconstruction, are discussed. Generally, the thermal field mapping is only applicable to cases where similar temperature curves are observed. The thermal field reconstruction could be applied to parts with any geometry and toolpath, whose accuracy depends on the amount of measured data and its training method. For future work, the generalization performance on metal parts with other geometries and toolpaths could be studied if more pyrometers or thermal cameras are available to measure the thermal field online. The extension of the proposed method to other metal additive manufacturing processes, e.g., laser powder bed fusion, and direct energy deposition, would be explored as well.

Declaration of competing interest

The authors declare that they have no known competing financial interests or personal relationships that could have appeared to influence the work reported in this paper.

Acknowledgements

The authors gratefully acknowledge funding from the Natural Sciences and Engineering Research Council (NSERC) of Canada [Grant numbers: RGPIN-2019-06601] and Business Finland under Project #: 4819/31/2021 with affiliation to the Eureka! SMART project (S0410) titled “TANDEM: Tools for Adaptive and Intelligent Control of Discrete Manufacturing Processes.”

References

[1] Dunbar AJ, Denlinger ER, Heigel J, Michaleris P, Guerrier P, Martukanitz R, et al. Development of experimental method for in situ distortion and temperature measurements during the laser powder bed fusion additive manufacturing process. Addit Manuf 2016;12:25–30. https://doi.org/10.1016/j.addma.2016.04.007.
[2] Panicker S, Nagarajan HPN, Tuominen J, Patnamsetty M, Coatanéa E, Haapala KR, et al. Investigation of thermal influence on weld microstructure and mechanical properties in wire and arc additive manufacturing of steels. Mater Sci Eng A 2022; 853:143690. https://doi.org/10.1016/j.msea.2022.143690.
[3] Mozaffar M, Paul A, Al-Bahrani R, Wolff S, Choudhary A, Agrawal A, et al. Data-driven prediction of the high-dimensional thermal history in directed energy deposition processes via recurrent neural networks. Manuf Lett 2018;18:35–9. https://doi.org/10.1016/j.mfglet.2018.10.002.
[4] Fetni S, Pham QDT, Tran VX, Duchêne L, Tran HS, Habraken AM. Thermal field prediction in DED manufacturing process using Artificial Neural Network. ESAFORM 2021 - 24th Int Conf Mater Form 2021. https://doi.org/10.25518/esaform21.2812.
[5] Pham TQD, Hoang TV, Pham QT, Huynh TP, Tran VX, Fetni S, et al. Data-driven prediction of temperature evolution in metallic additive manufacturing process. In: ESAFORM 2021 - 24th Int Conf Mater Form; 2021. https://doi.org/10.25518/esaform21.2599.
[6] Ness KL, Paul A, Sun L, Zhang Z. Towards a generic physics-based machine learning model for geometry invariant thermal history prediction in additive manufacturing. J Mater Process Technol 2022;302:117472. https://doi.org/10.1016/j.jmatprotec.2021.117472.
[7] Ren K, Chew Y, Zhang YF, Fuh JYH, Bi GJ. Thermal field prediction for laser scanning paths in laser aided additive manufacturing by physics-based machine learning. Comput Methods Appl Mech Eng 2020;362:112734. https://doi.org/10.1016/j.cma.2019.112734.
[8] Liao S, Xue T, Jeong J, Webster S, Ehmann K, Cao J. Hybrid thermal modeling of additive manufacturing processes using physics-informed neural networks for

temperature prediction and parameter identification. Comput Mech 2023. https://doi.org/10.1007/s00466-022-02257-9.
[9] Paul A, Mozaffar M, Yang Z, Liao WK, Choudhary A, Cao J, et al. A real-time iterative machine learning approach for temperature profile prediction in additive manufacturing processes. In: Proc - 2019 IEEE Int Conf Data Sci Adv Anal DSAA 2019; 2019. p. 541–50. https://doi.org/10.1109/DSAA.2019.00069.
[10] Zhou Z, Shen H, Liu B, Du W, Jin J. Thermal field prediction for welding paths in multi-layer gas metal arc welding-based additive manufacturing: a machine learning approach. J Manuf Process 2021;64:960–71. https://doi.org/10.1016/j.jmapro.2021.02.033.
[11] Stathatos E, Vosniakos GC. Real-time simulation for long paths in laser-based additive manufacturing: a machine learning approach. Int J Adv Manuf Technol 2019;104:1967–84. https://doi.org/10.1007/s00170-019-04004-6.
[12] Mozaffar M, Liao S, Lin H, Ehmann K, Cao J. Geometry-agnostic data-driven thermal modeling of additive manufacturing processes using graph neural networks. Addit Manuf 2021;48:102449. https://doi.org/10.1016/j.addma.2021.102449.
[13] Roy M, Wodo O. Data-driven modeling of thermal history in additive manufacturing. Addit Manuf 2020;32:101017. https://doi.org/10.1016/j.addma.2019.101017.
[14] Rahmani Dehaghani M, Tang Y, Panicker S, Wu D, Coatanea E, Wang GG. Modeling and optimization of height-related geometrical parameters for thin wall structures manufactured by metal additive manufacturing. Int J Adv Manuf Technol 2023. https://doi.org/10.1007/s00170-023-12618-0.
[15] Yildiz AS, Davut K, Koc B, Yilmaz O. Wire arc additive manufacturing of high-strength low alloy steels: study of process parameters and their influence on the bead geometry and mechanical characteristics. Int J Adv Manuf Technol 2020;108:3391–404. https://doi.org/10.1007/s00170-020-05482-9.
[16] Rodriguez N, Vázquez L, Huarte I, Arruti E, Tabernero I, Alvarez P. Wire and arc additive manufacturing: a comparison between CMT and TopTIG processes applied to stainless steel. Weld World 2018;62:1083–96. https://doi.org/10.1007/s40194-018-0606-6.
[17] Rodrigues TA, Duarte V, Avila JA, Santos TG, Miranda RM, Oliveira JP. Wire and arc additive manufacturing of HSLA steel: effect of thermal cycles on microstructure and mechanical properties. Addit Manuf 2019;27:440–50. https://doi.org/10.1016/j.addma.2019.03.029.
[18] Le VT, Mai DS, Doan TK, Paris H. Wire and arc additive manufacturing of 308L stainless steel components: optimization of processing parameters and material properties. Eng Sci Technol an Int J 2021;24(4):1015–26. https://doi.org/10.1016/j.jestch.2021.01.009.
[19] Bohler 3D PrintAM70, low-alloyed, high strength steel, Material Safety Data Sheet. >https://www.vabw-service.com/documents/boehler/datenblaetter/en/L1_34551_en_3Dprint_AM_70_1H43C006_3367515_EN (1).pdf?cache=1639059520. [Accessed 21 August 2023].
[20] Langsda Metal Products Co. Ltd, S355 alloy steel. https://www.inewsteel.com/product/S355-Alloy-Steel.html. [Accessed 21 August 2023].
[21] Bakrani Balani S, Mokhtarian H, Coatanéa E, Chabert F, Nassiet V, Cantarel A. Integrated modeling of heat transfer, shear rate, and viscosity for simulation-based characterization of polymer coalescence during material extrusion. J Manuf Process 2023;90:443–59. https://doi.org/10.1016/j.jmapro.2023.02.021.
[22] Veiga F, Suárez A, Artaza T, Aldalur E. Effect of the heat input on wire-arc additive manufacturing of invar 36 alloy: microstructure and mechanical properties. Weld World 2022;66:1081–91. https://doi.org/10.1007/s40194-022-01295-4.
[23] Rosli NA, Alkahari MR, bin Abdollah MF, Maidin S, Ramli FR, Herawan SG. Review on effect of heat input for wire arc additive manufacturing process. J Mater Res Technol 2021;11:2127–45. https://doi.org/10.1016/j.jmrt.2021.02.002.
[24] Hovakimyan N, Cause AJ, Kim N. Adaptive output feedback control of a class of multi-input multi-output systems using neural networks. Int J Control 2004;77(15):1318–29. https://doi.org/10.1080/00207170420002971 53.
[25] Raza SEA, Cheung L, Epstein D, Pelengaris S, Khan M, Rajpoot NM. MIMO-Net: a multi-input multi-output convolutional neural network for cell segmentation in fluorescence microscopy images. Proc Int Symp Biomed Imaging 2017:337–40. https://doi.org/10.1109/ISBI.2017.7950532.
[26] Zandie M, Ng HK, Gan S, Muhamad Said MF, Cheng X. Multi-input multi-output machine learning predictive model for engine performance and stability, emissions, combustion and ignition characteristics of diesel-biodiesel-gasoline blends. Energy 2023;262:125425. https://doi.org/10.1016/j.energy.2022.125425.
[27] Bischl B, Binder M, Lang M, Pielok T, Richter J, Coors S, et al. Hyperparameter optimization: foundations, algorithms, best practices, and open challenges. Wiley Interdiscip Rev Data Min Knowl Discov 2023;13:1–43. https://doi.org/10.1002/widm.1484.
[28] He K, Zhang X, Ren S, Sun J. Deep residual learning for image recognition. Proc IEEE Comput Soc Conf Comput Vis Pattern Recognit 2016:770–8. https://doi.org/10.1109/CVPR.2016.90.
[29] Kingma DP, Ba JL. Adam: a method for stochastic optimization. 3rd Int Conf Learn Represent ICLR 2015 - Conf Track Proc; 2015. https://doi.org/10.48550/arXiv.1412.6980.
[30] Paszke A, Gross S, Massa F, Lerer A, Bradbury J, Chanan G, et al. PyTorch: an imperative style, high-performance deep learning library. Adv Neural Inf Proces Syst 2019:32. https://doi.org/10.5555/3454287.3455008.
[31] Yu J, Yan C, Guo M. Non-intrusive reduced-order modeling for fluid problems: a brief review. Proc Inst Mech Eng Part G J Aerosp Eng 2019;233:5896–912. https://doi.org/10.1177/0954410019890721.
[32] Kerschen G, Golinval JC, Vakakis AF, Bergman LA. The method of proper orthogonal decomposition for dynamical characterization and order reduction of mechanical systems: an overview. Nonlinear Dyn 2005;41:147–69. https://doi.org/10.1007/s11071-005-2803-2.
[33] Hua J, Sørheim EA. Nonintrusive reduced-order modeling approach for parametrized unsteady flow and heat transfer problems. Int J Numer Methods Fluids 2022;94:976–1000. https://doi.org/10.1002/fld.5080.
[34] Kadeethum T, Ballarin F, Choi Y, O'Malley D, Yoon H, Bouklas N. Non-intrusive reduced order modeling of natural convection in porous media using convolutional autoencoders: comparison with linear subspace techniques. Adv Water Resour 2022;160:104098. https://doi.org/10.1016/j.advwatres.2021.104098.
[35] Park K, Allen MS. A Gaussian process regression reduced order model for geometrically nonlinear structures. Mech Syst Signal Process 2023;184:109720. https://doi.org/10.1016/j.ymssp.2022.109720.
[36] Lu K, Zhang K, Zhang H, Gu X, Jin Y, Zhao S, et al. A review of model order reduction methods for large-scale structure systems. Shock Vib 2021;2021. https://doi.org/10.1155/2021/6631180.
[37] Huang GB, Zhu QY, Siew CK. Extreme learning machine: theory and applications. Neurocomputing 2006;70:489–501. https://doi.org/10.1016/j.neucom.2005.12.126.
[38] Wang J, Lu S, Wang SH, Zhang YD. A review on extreme learning machine. Multimed Tools Appl 2021;81:41611–60. https://doi.org/10.1007/s11042-021-11007-7.
[39] Leung HC, Leung CS, Wong EWM. Fault and noise tolerance in the incremental extreme learning machine. IEEE Access 2019;7:155171–83. https://doi.org/10.1109/ACCESS.2019.2948059.
[40] Ma Z, Luo G, Huang D. Short term traffic flow prediction based on on-line sequential extreme learning machine. In: Proc 8th Int Conf Adv Comput Intell ICACI 2016. 2; 2016. p. 143–9. https://doi.org/10.1109/ICACI.2016.7449818.
[41] Kouzehkalani Sales A, Gul E, Safari MJS. Online sequential, outlier robust, and parallel layer perceptron extreme learning machine models for sediment transport in sewer pipes. Environ Sci Pollut Res 2023;30(14):39637–52. https://doi.org/10.1007/s11356-022-24989-0.
[42] Weng F, Chen Y, Wang Z, Hou M, Luo J, Tian Z. Gold price forecasting research based on an improved online extreme learning machine algorithm. J Ambient Intell Humaniz Comput 2020;11:4101–11. https://doi.org/10.1007/s12652-020-01682-z.
[43] Li X. Extreme learning machine (ELM): Python code. https://github.com/5663015/elm. [Accessed 27 April 2023].
[44] Pandita P, Ghosh S, Gupta VK, Meshkov A, Wang L. Application of deep transfer learning and uncertainty quantification for process identification in powder bed fusion. ASCE-ASME J Risk Uncert Engrg Sys Part B Mech Engrg 2022;8(1):1–12. https://doi.org/10.1115/1.4051748.
[45] Sabbaghi A, Huang Q. Model transfer across additive manufacturing processes via mean effect equivalence of lurking variables. Ann Appl Stat 2018;12(4):2409–29. https://doi.org/10.1214/18-AOAS1158.
[46] Mehta M, Shao C. Federated learning-based semantic segmentation for pixel-wise defect detection in additive manufacturing. J Manuf Syst 2022;64:197–210. https://doi.org/10.1016/j.jmsy.2022.06.010.
[47] Tang Y, Rahmani Dehaghani M, Wang GG. Review of transfer learning in modeling additive manufacturing processes. Addit Manuf 2023;61:103357. https://doi.org/10.1016/j.addma.2022.103357.
[48] Pant P, Doshi R, Bahl P, Barati Farimani A. Deep learning for reduced order modelling and efficient temporal evolution of fluid simulations. Phys Fluids 2021:33. https://doi.org/10.1063/5.0062546.